

A NOVEL, FULLY AUTOMATED PIPELINE FOR PERIOD ESTIMATION IN THE EROS 2 DATA SET

PAVLOS PROTOPAPAS^{1,2}, PABLO HUIJSE^{3,4}, PABLO A. ESTÉVEZ^{4,3}, PABLO ZEGERS⁵, JOSÉ C. PRÍNCIPE⁶, JEAN-BAPTISTE MARQUETTE⁷

¹Institute for Applied Computational Science, Harvard University, Cambridge, MA, USA

²Harvard-Smithsonian Center for Astrophysics, 60 Garden Street, Cambridge, MA, USA

³Millennium Institute of Astrophysics, Chile

⁴Department of Electrical Engineering and the Advanced Mining Technology Center, Universidad de Chile, Santiago, Chile

⁵Universidad de los Andes, Facultad de Ingeniería y Ciencias Aplicadas, Monseñor Álvaro del Portillo 12455, Las Condes, Santiago, Chile

⁶Computational Neuroengineering Laboratory of University of Florida, FL, USA

⁷UPMC-CNRS, UMR7095, Institut d'Astrophysique de Paris, F-75014, Paris, France and
email: pavlos@seas.harvard.edu

Draft version November 21, 2018

ABSTRACT

We present a new method to discriminate periodic from non-periodic irregularly sampled lightcurves. We introduce a periodic kernel and maximize a similarity measure derived from information theory to estimate the periods and a discriminator factor. We tested the method on a dataset containing 100,000 synthetic periodic and non-periodic lightcurves with various periods, amplitudes and shapes generated using a multivariate generative model. We correctly identified periodic and non-periodic lightcurves with a completeness of $\sim 90\%$ and a precision of $\sim 95\%$, for lightcurves with a signal-to-noise ratio (SNR) larger than 0.5. We characterize the efficiency and reliability of the model using these synthetic lightcurves and applied the method on the EROS-2 dataset. A crucial consideration is the speed at which the method can be executed. Using hierarchical search and some simplification on the parameter search we were able to analyze 32.8 million lightcurves in ~ 18 hours on a cluster of GPGPUs. Using the sensitivity analysis on the synthetic dataset, we infer that 0.42% in the LMC and 0.61% in the SMC of the sources show periodic behavior. The training set, the catalogs and source code are all available in <http://timemachine.iic.harvard.edu>.

Subject headings: -

1. INTRODUCTION

Characterization of the dynamic optical sky is one of the observational frontiers in astrophysics. Variable sources, defined as any source that its apparent magnitude changes over time, have historically led to fundamental insights into subjects ranging from the structure of stars and the most energetic explosions in the universe to cosmology. These changes and their characteristics, tell us a lot about the sources such as pulsating stars, supernovae, the interaction of the source with its surrounding such as AGNs or light being blocked by something between the source and the observer. However no optical telescope to date has had the capability to search for transient phenomena at faint levels over enough of the sky to fully characterize variable sources.

A subcategory of the variable sources are the periodic variables. Those are variables that in general repeat at regular intervals. While astronomers historically have been able to study variable and transient phenomena by examining the behavior of individual sources, the amount of data and the large number of sources have exponentially grown in the last decade (Hodapp et al. 2004; Ivezić et al. 2011; Larson et al. 2003; Law et al. 2009), making this task daunting.

Although most stars have at least some variation in luminosity, current estimations indicate that 3% of the stars are varying more than the sensitivity of the instruments and $\sim 1\%$ are periodic (Eyer 1999). EROS-2 (Tisserand et al. 2007), MACHO (Alcock et al. 2000), OGLE (Udalski et al. 1997) were among the first genera-

tion of large scale surveys, monitoring millions of sources for many years. Pan-STARRS (Hodapp et al. 2004) is currently monitoring the whole visible sky repeatedly and it will be doing it for a total of three years. In the future SDSS (York et al. 2000), LSST (Ivezić et al. 2011) will monitor even more sources, and more frequently, generating billions of lightcurves. It is because of this explosion of data that there is a need for efficient and well characterized period finding techniques.

The problem of period estimation from noisy and irregularly sampled observations has been studied before. Most approaches identify the period by some form of grid search. That is, the problem is solved by evaluating a criterion Φ at a set of trial periods and selecting the period p that yields the best value for $\Phi(p)$. Commonly used techniques vary in the form and parametrization of Φ , the evaluation of the fit quality between model and data, the set of trial periods searched, and the complexity of the resulting procedures. Two methods that are popular are the LS periodogram (Scargle 1982; Reimann 1994) and the phase dispersion minimization (PDM) (Stellingwerf 1978), both known for their success in empirical studies. The LS method is relatively fast and is equivalent to maximum likelihood estimation under the assumption that the function has a sinusoidal shape. It therefore makes a strong assumption on the shape of the underlying function. On the other hand, PDM makes no such assumptions and is more generally applicable, but it is slower and is less often used in practice.

In this paper we adopted the correntropy kernelized periodogram (CKP), an information theoretical criterion

introduced in Huijse et al. (2012) to assess periodicity in lightcurves. The CKP combines the generalized autocorrelation function (Principe 2010) with a periodic kernel yielding a generalized periodogram. The CKP measures similarity over time using statistical information contained in the probability density function (pdf) of the samples. This gives the CKP an advantage over methods that rely on second-order statistical descriptors¹. By adjusting the kernel parameters of the CKP one can adapt the metric to different noise regimes and periodicities. The selection of these parameters for the case of lightcurves is thoroughly discussed in the present work.

To fully qualify the method we generated a large set of synthetic lightcurves (110K) using parameter distributions motivated from the data. To do so, we used a model free multivariate generative model and sampled the parameters. We also use a smaller but manageable subset from the real data in order to compare our results with reality. These subsets were used to optimize the free parameters of the pipeline and to characterize the efficiency and completeness of the process.

Astronomy and many experimental sciences are now collecting more data that can be possibly analyzed by human experts in reasonable time. We are not really interested in the data per se, but in the information it contains about the natural phenomena. Machine learning and signal processing are becoming an integral part of the process of extracting information from data, because they are quantitative methods based on statistics and function analysis methods. This synergism is in its early stages, and this paper shows an effective methodology to speed up the discovery of periodic stars in large data bases as the EROS2.

Section 2 describes the theoretical framework that this work is based on, Section 3 describes the pipeline and methodology, Section 4 describes the synthetic data set, Section 5 describes the data, Section 6 contains the results obtained from our runs and finally conclusions are in Section 9.

2. THEORETICAL FRAMEWORK

The structure of a time series can be quantified by measuring the signal similarity over time. The first measure that comes to mind is the autocorrelation function of the time series (Jenkins & Watts 1968). Let us define the time series as a realization of a stochastic process $\{x_n, n = 0, 1, \dots, N\}$, where x is a random variable in \mathbb{R} . The autocorrelation function for stationary processes is defined as

$$R[m] = \mathbb{E}[\langle x_n, x_{n-m} \rangle], \quad (1)$$

where $\mathbb{E}[\cdot]$ indicates the expectation value. The autocorrelation coefficient² normally is estimated for stationary and ergodic time series as a simple sum of lagged products over a window of data.

$$\hat{R}[m] = \frac{1}{N+1-m} \frac{1}{\sigma^2} \sum_{n=m}^N (x_n - \mu)(x_{n-m} - \mu), \quad (2)$$

¹ To fully characterize non-gaussian random processes the higher order moments are needed.

² Covariance normalized by the variance

where $N+1$ is the number of measurements in the time series and the true mean μ and true variance σ^2 are time-independent.

Looking more closely at the autocorrelation definition one finds out that only second order information of the random variable x is utilized in the definition, and as it is well known, only a few distributions such as the Gaussian are fully described by their (first and) second order moments. Therefore, one compromises the simplicity of the autocorrelation definition with a loss of a more in depth description of the signal similarity. This paper will use more powerful definitions of similarity for a better quantification of time series structure, which is pivotal to achieve the reported results. The ideas are founded in the mathematical theory of information and a descriptor of entropy that exploits the full statistical information from samples (Principe 2010), which is utilized to define similarity metrics.

Let us consider a stationary stochastic process $\{x_n\}$, and define the generalized autocorrelation as

$$V[m] = \mathbb{E}[\kappa(x_n, x_{n-m})], \quad (3)$$

where $\kappa(x, y)$ is a positive definite function of two arguments called a kernel (Schölkopf & Smola 2002; Taylor & Cristianini 2004). If we define $\kappa(x, y) = \langle x, y \rangle$, i.e. the first order polynomial kernel one obtains the autocorrelation function of Eq. (1), (2). Instead let us select $\kappa(x, y)$ as a translation invariant kernel (Schölkopf & Smola 2002), i.e. $\kappa(x, y) = \kappa(x - y, 0)$. For simplicity we will use $\kappa(x - y)$ for translation-invariant kernel functions. The Gaussian kernel defined as

$$G_\sigma(x - z) = \frac{1}{\sqrt{2\pi}\sigma} \exp\left(-\frac{\|x - z\|^2}{2\sigma^2}\right), \quad (4)$$

is a popular kernel that fits the conditions, where σ is the covariance, and will be called in this context as *the kernel size*. In Principe (2010) this class of functions is called autocorrentropy, or more simply correntropy, and here we will always assume the use of the Gaussian kernel. One of the advantages of correntropy is that it is still very easy to estimate directly from data assuming the random process is ergodic. Using the sample mean we can estimate Eq. (3) as

$$\hat{V}_\sigma[m] = \frac{1}{N+1-m} \sum_{n=m}^N G_\sigma(x_n - x_{n-m}). \quad (5)$$

The difference between autocorrelation and autocorrentropy seems pretty minor, but it is very significant, as fully discussed in Principe (2010). For this work, the important correntropy properties are the following:

1. Correntropy with the Gaussian kernel includes a weighted sum of all the even moments of the random variable, including the second order moment (the autocorrelation) of $\|x_n - x_{n-m}\|$.
2. Correntropy is a positive definite function can replace the autocorrelation function in the definition of the Power spectrum, yielding the correntropy spectral density (CSD) (Principe 2010), as

$$P_\sigma[f] = \sum_{m=-\infty}^{\infty} U_\sigma[m] \cdot \exp\left(-i2\pi f \frac{m}{F_s}\right), \quad (6)$$

where F_s corresponds to the sampling frequency. The function $U_\sigma[m]$ corresponds to $V_\sigma[m] - IP$, where IP corresponds to the mean value of the autocorrentropy function over the lags³.

3. Correntropy has a free parameter that can be interpreted as a scale parameter, therefore needs to be defined according to the time series data.
4. Correntropy quantifies similarity using the correntropy induced metric (CIM) defined as

$$CIM(x, y) = (\kappa(0, 0) - \mathbb{E}[\kappa(x, y)])^{1/2}. \quad (7)$$

The CIM is a metric very different from the L_p norms that define the Minkowski spaces where the distances are always weighted the same (Fig 1)⁴. This means that distances between the arguments of the CIM are weighted nonuniformly, i.e. if the distance between the arguments is small then the CIM approximates the L_2 norm, but if the difference is larger then it will approximate the L_1 norm, and for very large difference between the arguments, the CIM tends to the L_0 norm. The transitions between the norms are smooth, and the assessment of ‘small’ and ‘large’, the scale in this space is controlled by the kernel size, which impacts drastically the assessment of similarity.

It is appropriate to present a synthetic example to illustrate the difference between autocorrelation and autocorrentropy in assessing similarity over time, and also to elucidate the role of the kernel size. Let us take the case of the stochastic process with uniform random amplitude in $[-A, A]$ and a random phase in $[-\pi, \pi]$ defined as $x_n = A \sin(w_0 n + \varphi)$. As it is well known, the autocorrelation function of sinewaves is a sinewave with the same period. But should it be a sinewave if we are interested in assessing the degree of similarity of the signal time structure? Since the sinewave is periodic, the similarity is maximum when the delay is exactly one period, but for intermediate shifts, the two functions are very dissimilar, and autocorrelation does not show this very clearly (and the similarity is not normalized nor always positive, hence the use of the correlation coefficient). Therefore, if we are seeking a discriminative measure of similarity, the autocorrelation function is not exploiting optimally the information available in the statistics of the data. It turns out that correntropy is more discriminative, as shown in Fig 2. The autocorrentropy of a sinewave (or any other periodic function) is a periodic pulse train defined by the data period, where the pulses can be made arbitrarily sharp by decreasing the kernel size to zero. This can be easily explained by observing Eq. (5). When x_n and x_{n-m} are similar the argument is close to zero and the Gaussian yields a value close to the argument square; when the difference increases, the Gaussian function produces exponentially smaller results proportional to the

difference in arguments ; and for larger differences, the Gaussian gives back very small values close to zero (see Fig 1a). Of course if white noise is added to the sinewave, one immediately sees that the kernel size can not be made arbitrarily small, otherwise the correntropy becomes always very small, not capturing the periodic nature of the noisy signal. But if the kernel size needs to be made very large to accommodate large noises, then the autocorrentropy approaches the autocorrelation function.

2.1. Periodic kernel

With this introduction in mind, we move on specifying the kernel that best encapsulates the information in the data for periodic signals. Periodic kernel functions are known to be appropriate for nonparametric estimation, modelling and regression of periodic time series (Michalak 2010). A kernel function is periodic with period P if it repeats itself for inputs separated by P . Periodic kernel functions have also been proposed in the Gaussian processes literature (Rasmussen & Williams 2006; Mackay 1998; Wang et al. 2012).

A periodic kernel function can be obtained by applying a nonlinear mapping (or warping) $u(t)$ to the input vector t . In Mackay (1998) a periodic kernel function was constructed by mapping a unidimensional input variable t using a periodic two-dimensional warping function defined as

$$u_f(t) = (\cos(2\pi ft), \sin(2\pi ft)).$$

The periodic kernel function $G_\sigma^P(f, t_z - t_y)$ with period $1/f$, is obtained by applying this warping function to the inputs of the Gaussian kernel function (Eq. 4). The periodic kernel function is defined as:

$$G_\sigma^P(f, t_z - t_y) = G_\sigma(u_f(t_z) - u_f(t_y)) \quad (8) \\ = \frac{1}{\sqrt{2\pi}\sigma} \exp\left(-\frac{2 \sin^2(\pi f(t_z - t_y))}{\sigma^2}\right),$$

where the following expression is used

$$\|u_f(z) - u_f(y)\|^2 = 4 \sin^2(\pi f(z - y)).$$

Note that the periodic kernel is a function $\delta t = (t_z - t_y)$ and frequency, the inverse of the period. The Taylor series expansion at $\delta t = 0$ of Eq. (8) is defined as

$$G_\sigma^P(f, \delta t) = \lim_{N \rightarrow \infty} \quad (9) \\ \sum_{k=0}^N \frac{(-1)^k}{k! \sigma_t^{2k} 2^{k-1}} \left[\sum_{m=0}^k \binom{2k}{k-m} (-1)^m g_m \cos(2\pi m f \delta t) \right],$$

where

$$g_m = \begin{cases} 1/2, & \text{if } m = 0. \\ 1, & \text{otherwise.} \end{cases}$$

Note that for large values of σ , only the first terms contribute to the sum and thus the periodic kernel tends to a constant plus $\cos(2\pi f \delta t)$, which corresponds to the real part of the Fourier basis.

³ This also the argument of Renyi’s quadratic entropy (Principe 2010).

⁴ For $\vec{x} \in \mathbb{R}^n$, the L_p norms are defined as $L_p = \|\vec{x}\|_p = \left(\sum_{i=1}^n x_i^p\right)^{1/p}$, $p \in (0, \infty)$. In the limit $p \rightarrow 0$, the L_0 norm is defined as the number of non-zero components in the vector (counting norm).

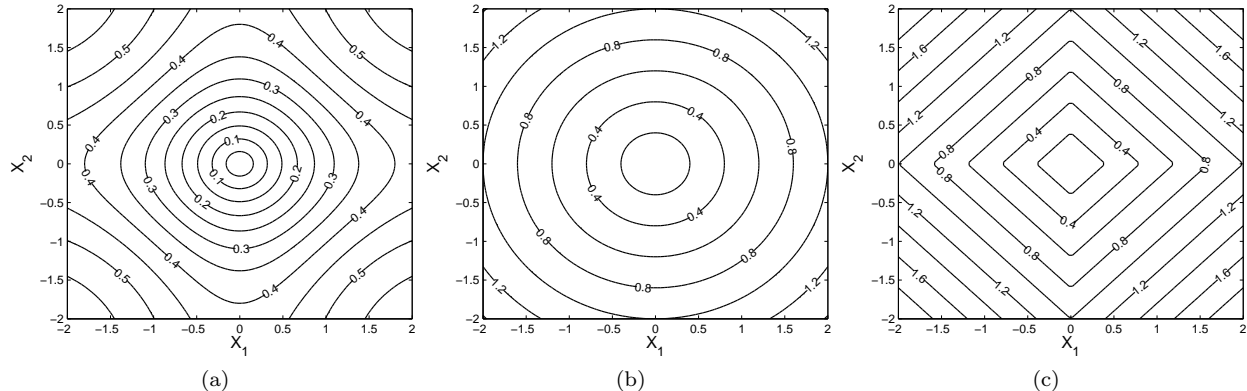


FIG. 1.— Distances to the origin (contours) in a bidimensional sample space using the CIM(X,0) (a), L_2 norm (b) and L_1 norm (c). For the CIM (Eq. 7) a Gaussian kernel function with $\sigma = 1$ is considered. Note how the CIM incorporates the L_1 , L_2 and L_0 norms at different scales.

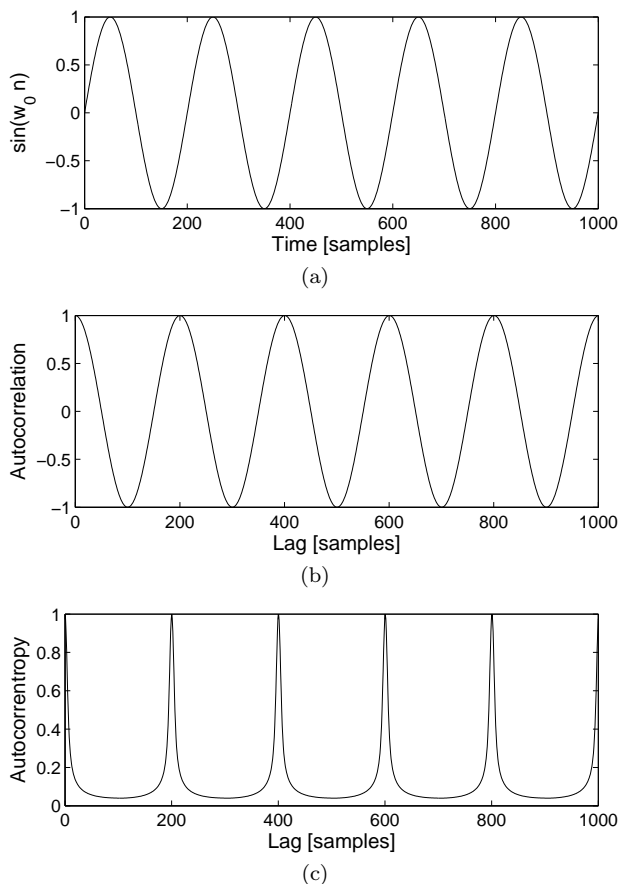


FIG. 2.— (a) Plot of $x_n = A \sin(w_0 n + \varphi)$ with unit amplitude, $w_0 = 2\pi/200$ and where φ is a random variable uniformly distributed in $[-\pi, \pi]$. (b) Autocorrelation of x_n , note that the autocorrelation function of a sinewave is a sinewave. (c) Autocorrentropy of x_n , note that the autocorrentropy of a sinewave is a train pulse in which the periodicity is represented by the peaks. The sharpness of the peaks can be controlled using σ .

3. METHOD

We base our methodology on the work described in Huijse et al. (2012). In this section we summarize the key points from that work, then introduce the new concepts, particularly an intuitive interpretation of the parameters of the CKP, simple rules to select these parameters and a normalization term that is needed to perform ensemble comparisons.

The correntropy kernelized periodogram (CKP) used in Huijse et al. (2012) is a period detection function developed for unevenly sampled time series. The CKP is computed from the available samples following a direct quadratic estimator approach as proposed in Marquardt & Acuff (1984)⁵. For a discrete unidimensional random process $\{x_n, n = 1, \dots, N\}$ with kernel sizes σ_t and σ_y , and a period $1/f$, the CKP is computed as:

$$\text{CKP}_{\{\sigma_t, \sigma_y\}}(f) = \quad (10)$$

$$\frac{1}{N^2} \sum_{i=1}^N \sum_{j=1}^N (G_{\sigma_y}(\Delta y_{ij}) - IP_{\sigma_y}) G_{\sigma_t}^P(f, \Delta t_{ij}),$$

where $\Delta y_{ij} = y_i - y_j$, $\Delta t_{ij} = t_i - t_j$, $G_{\sigma_y}(\cdot)$ is the Gaussian kernel function (Eq. 4), $G_{\sigma_t}^P(\cdot, \cdot)$ is the periodic kernel function (Eq. 8), and IP_{σ_y} is the information potential

$$IP_{\sigma_y} = \frac{1}{N^2} \sum_{i=1}^N \sum_{j=1}^N G_{\sigma_y}(\Delta y_{ij}). \quad (11)$$

Note that Eq. (10) is similar to the CSD (Eq. 6) with two main differences: a) the CKP is estimated in a direct approach and b) the basis functions, $\exp(-i2\pi f m / F_s)$ have been replaced by the periodic kernel (Eq. 8). In this sense the CKP can be interpreted as the result of transforming the autocorrentropy function through a basis defined by the periodic kernel.

By comparing magnitude values through the autocorrentropy function, the CKP is effectively using a CIM (Eq. 7) metric to measure magnitude distances. The kernel size σ_y has influence in the assessment of magnitude similarities as explained in the previous section. The CKP compares time differences with the trial period through the periodic kernel. The periodic kernel size σ_t allows the user to choose how this comparison is made.

By summing in the time and magnitude index, a function of the trial period is obtained, thus the CKP can be considered a generalized periodogram. Consequently, in order to detect periods in lightcurves the CKP is maximized over the frequency (inverse of the period) for a

⁵ The basic idea is that for uneven samples, one can calculate the periodogram without having to regularize the data.

given combination of parameters, namely the two kernel bandwidths (σ_y, σ_t).

One of the major advantages of the CKP over conventional methods is its adaptability given by the kernel parameters. In what follows, we describe heuristic approaches that use the available information on the lightcurve to set the kernel sizes. Without them the maximization of the CKP would have been a very expensive procedure.

★ The kernel bandwidth, σ_y , controls the observation window that is used to compare the magnitude values of the lightcurve. This parameter needs to be set small enough so that outliers are filtered, but large enough to compensate for the observational and other measurements errors. Conveniently those errors are usually available for most measurements in lightcurves (these are the magnitude errors). For a given lightcurve the Gaussian kernel bandwidth is selected as

$$\sigma_y = \text{med}(\{e\}), \quad (12)$$

where med is the median, and $\{e\}$ are the error bars of the measurements in lightcurve. Fig. 3a shows a synthetic periodic lightcurve with random error bars. Samples y_1 and y_2 are compared using the Gaussian kernel, where the median of the error bars is 0.08 and the σ_y is set to be 0.08. Fig. 3b shows the equivalent Gaussian kernel value for this pair. In reality the observational errors are not constant and therefore eq. 12 should not be the same for all pairs and should be a combination of the two observational errors added in quadrature. Practically the difference of this approximation and the correct approach is insignificant.

★ The kernel bandwidth, σ_t , controls the observation window that is used to compare the time differences of the lightcurve with the trial period. When $\sigma_t \rightarrow 0$ only the samples whose time differences are equal to the trial period will be picked by the periodic kernel. The smaller the σ_t is, the more precise the estimation will be, although in practice fewer samples will be available. When σ_t grows large, the exponential in Eq. (8) takes less relevance and the periodic kernel tends to a sinusoidal function⁶. Intuitively, this parameter has influence on the periodicity's shape. A smaller σ_t is beneficial to pick up shapes that have many features or abrupt changes, such as the narrow eclipses of an Algol-type eclipsing binary. On the contrary a large σ_t is used for smoother shapes, *i.e.* wiggles and high derivatives are ignored. In summary the σ_t needs to be set small enough so that the features of the periodicity will not be missed, but large enough so that there will be enough samples representing the period and to avoid picking up structures due to the noise.

Since σ_t describes the smoothness of the shape of the lightcurve, a way to estimate σ_t is to find the variation of δt 's in a given y-band. Empirically, we observed that for almost all periodic lightcurves, the CKP is maximized for $\sigma_t \sim 0.1 - 0.6$ and that the value of σ_t is strongly correlated with the third moment or the skewness of the distribution of the magnitudes of the lightcurves. Lightcurves with skewed distributions, such as those corresponding

to eclipsing binaries (Fig. 4a), get a small σ_t value. On the other hand, lightcurves with very symmetric distributions (Fig. 4b) will get a larger σ_t . Finally, we will address ensemble comparisons for period discrimination. The kernel sizes are selected for each lightcurve differently as described above and in order to compare different lightcurves, the CKP is required to be invariant under σ_y, σ_t and the sample size.

For that we propose a properly normalized CKP metric as:

$$\text{nCKP}_{\{\sigma_t, \sigma_y\}}(f) = \quad (13)$$

$$\frac{\sqrt{N\sigma_t}}{IP_{\sigma_y}} \frac{1}{N^2} \sum_{i=1}^N \sum_{j=1}^N (G_{\sigma_y}(\Delta y_{ij}) - IP_{\sigma_y}) G_{\sigma_t}^P(f, \Delta t_{ij}),$$

where $1/IP_{\sigma_y}$ normalizes against σ_y , $\sqrt{\sigma_t}$ normalizes against σ_t and \sqrt{N} normalizes against the number of samples. The normalization factors were confirmed empirically by comparing the distribution of the CKP across different sets of surrogate lightcurves, generated with the procedures described in Section 4. Fig. 5a shows a histogram of $\max \text{CKP}_{\{\sigma_t, \sigma_y\}}(f)$ for three sets of surrogates generated with different N values. In this figure the unnormalized CKP is used (Eq. 10). For the histogram shown in Fig. 5b the normalized CKP (Eq. 13) is used, in this case the distribution of the CKP is equivalent, thus it is invariant to the different N of the surrogates.

3.1. Trial period extraction, the bands method

The parameter to be estimated by maximizing the CKP is the period. Unfortunately the dependence of CKP on period is not uniform and difficult to model (Huijse et al. 2012), therefore any clever optimization technique fails to converge faster than the brute force approach.

To alleviate this problem, a fast search algorithm is adopted. The basic idea is that two points in an ideal lightcurve having the same magnitude, have to be apart in time by an integer multiple of the period. For the ideal lightcurve case, finding the period is as simple as finding the greatest common divisor of the times of two points with the same magnitude⁷. However, the ideal case is not applicable to astronomical data because: a) lightcurves comprise of a nominal part and a signal part as in the case of planetary transits and eclipsing binaries, b) the observations are not performed continuously and c) measurements are not perfect but suffer from observational errors.

What follows, is an approximation tailored for real lightcurves. Instead of looking at pairs of points with the same magnitude, subsets of points with similar magnitudes are selected. These subsets, called bands, should contain points that have time differences that are multiples of the period, and therefore, in Fourier space these periods are enhanced. To avoid bands that the lightcurve is in its nominal state we select bands where the derivatives are higher.

The details of the method are as:

For an unidimensional time series $\{t_i, x_i\}$ with $i = 1, \dots, N$

⁶ As shown in Section 2.1 through the Taylor expansion of Eq. (8).

⁷ This is the famous Euclid algorithm (oldest known).

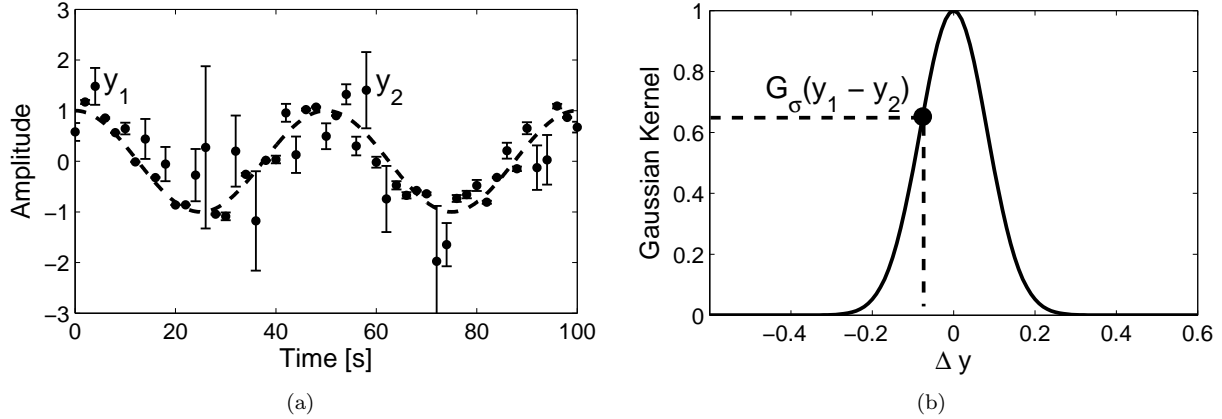


FIG. 3.— (a) Periodic synthetic time series $\cos(2\pi ft) + N(0, 0.5)$, the dotted line corresponds to the underlying signal. In this example the median of the errorbars is 0.08. Samples y_1 and y_2 are compared using the Gaussian kernel (b). The kernel size is set to 0.08.

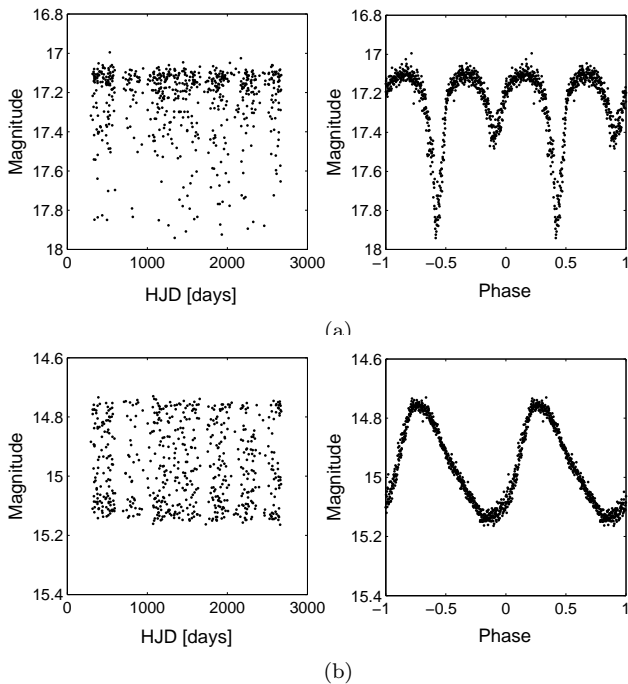


FIG. 4.— (a) lightcurve lm009017821 folded with a period of 1.4255 days. This lightcurve has a highly positive skewed distribution. A time kernel bandwidth of $\sigma_t = 0.115$ is selected for this lightcurve. (b) lightcurve lm0090n9337 folded with a period of 4.3949 days. This lightcurve has a symmetric distribution. In this case a time kernel bandwidth of 0.475 is selected.

- Compute the first derivatives $d_i = \frac{x_{i+1} - x_i}{t_{i+1} - t_i}$.
- Divide the ordinate axis in 10 uneven-width bands, such that each band has a 10% of the lightcurve samples.
- Compute the sum of the first derivatives that belong to band- j (B_j), $D_j = \sum_{i \in B_j} |d_i|$, with $j = 1, \dots, 10$.
- Sort the bands in descending order of D_j and keep the first N_b bands.
- For each band compute the spectral window function (Jenkins & Watts 1968) on a linearly spaced frequency grid from 0.00125 1/days to 3 1/days

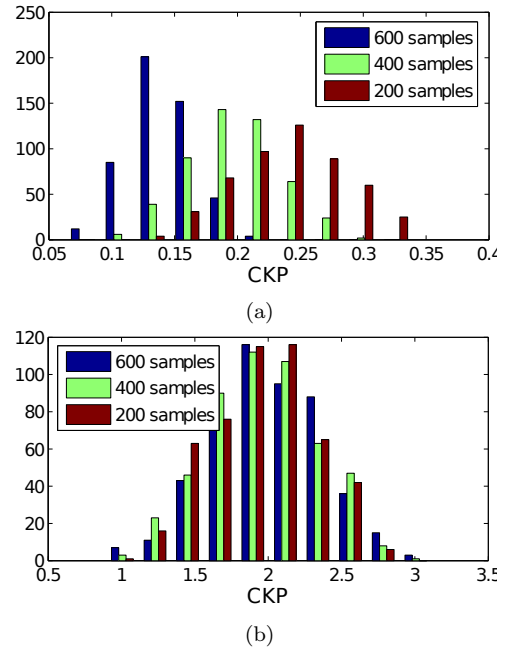


FIG. 5.— Distribution of the maximum CKP values on a set of 1500 synthetic light curves. The light curves are generated with the same period and SNR but using different number of samples (N). Three sets of 500 light curves are generated using 200, 400 and 600 number of samples, respectively. Fig (a) shows the distribution of the unnormalized CKP. It is clear the CKP is not invariant to N . Light curves with higher N have higher CKP values. Fig (b) shows the distribution of the normalized CKP.

(periods between 0.3 days and 800 days),

$$S_j(f) = \left| \sum_{i \in B_j} \exp(j2\pi f t_i) \right|^2 \quad (14)$$

- Save the frequencies associated with the N_t highest local maxima of $S_j(f)$. Periods that comply with $\|P - 1\| < 1e - 4$ are omitted⁸. This gives a total of $N_b N_t$ trial frequencies.
- The number of analyzed bands, N_b , and the amount of trial periods extracted per band, N_t , are user defined

⁸ The one day pseudo sampling period is strongly represented in all the bands.

parameters, that represent a trade-off between efficiency and computational time. We expect to find the correct period in the first sorted bands, however the true period may be captured by different bands although with different amplitudes, *i.e.* the rank of true period may vary across bands. For example the true period may be ranked 100th in the first band and 10th in the third band. Synthetic lightcurves (see Section 4) are analyzed with the period detection pipeline using different combinations of N_t and N_b .

Fig. 6 shows a contour plot of the hit rate as a function of N_b and N_t . As expected, hit rates increase with N_b and N_t . For every N_t , the hit rate **gain** obtained by adding additional bands decreases with N_b , which indicates that the bands are correctly sorted. Fig. 7 shows a contour plot of the computational time required to analyze one lightcurve as a function of N_b and N_t . For two points with equal $N_b N_t$ the point with lower N_b requires less computational time. In terms of computational time, adding bands is less desirable than increasing N_t . The maximum hit rate achieved is 98.1%. We find the best operation point to be $N_b = 3$ and $N_t = 150$, which yields a hit rate of 95.1% with a computational time of 0.162s per lightcurve. This point represent the best compromise between efficiency and computational time and is found by maximizing $HR + 1/c_t$, where c_t is the computational time.

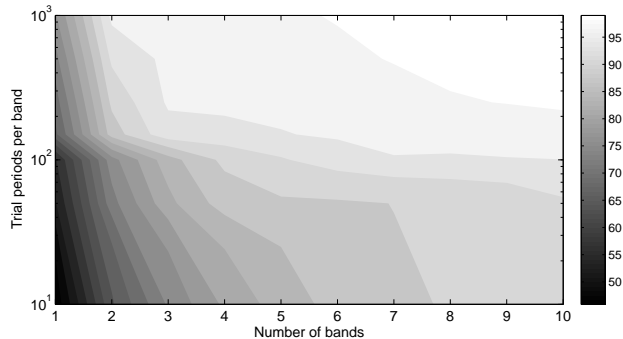


FIG. 6.— Hit rate as a function of the parameters of the bands methods. These parameters are the number of bands N_b and the number of trial periods extracted per band N_t .

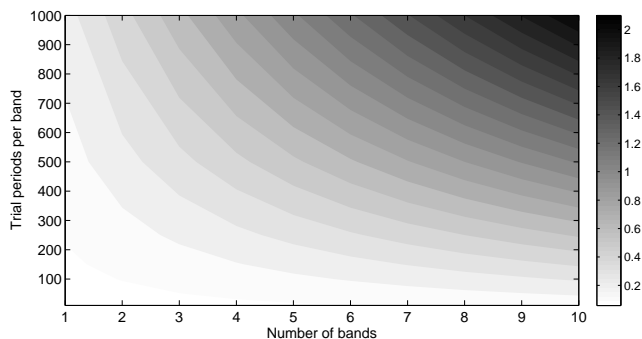


FIG. 7.— Computational time in seconds required to process one lightcurve (600 samples) as a function of the parameters of the bands methods. These parameters are the number of bands N_b and the number of trial periods extracted per band N_t .

Fig. 8a shows a plot of an EROS-2 lightcurve, lm0090m4818. Fig. 8b shows the same lightcurve folded

with a period of 1.54192 days. The black dotted lines mark the band divisions on the magnitude axis. The shaded region shows the best band in terms of the first derivatives criterion. Fig. 9 shows a plot of the spectral window function of the time instants extracted from the best band of lm0090m4818. The true period of the lightcurve is associated with the eighth highest local maximum of the spectral window. In this case, if $N_t > 8$ then the underlying period will be within the trial period set that is to be evaluated by the CKP in the next step of the pipeline.

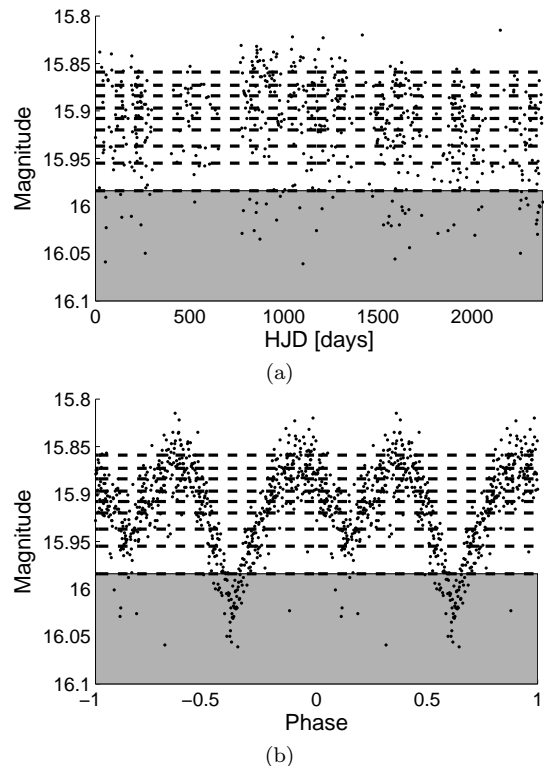


FIG. 8.— (a) EROS-2 lightcurve lm0090m4818. The dotted lines show the band divisions. The shaded region shows the best band in terms of the first derivatives criterion. (b) Same lightcurve folded with a period of 1.54192 days.

3.2. Performance criteria

The task of discriminating periodic lightcurves can be viewed as a binary classification problem where the classes are periodic (true) and non-periodic (false) lightcurves. In this case: true positives (TP) are the periodic lightcurves classified as periodic, false positive (FP) are the non-periodic lightcurves classified as periodic, true negative (TN) are the non-periodic lightcurves classified as non-periodic and false negative (FN) are the periodic lightcurves classified as non-periodic.

To evaluate the performance of our method we use the definitions of recall, r , precision p

$$r = \frac{\text{TP}}{\text{TP} + \text{FN}}, \quad p = \frac{\text{TP}}{\text{TP} + \text{FP}} \quad (15)$$

and F-score

$$F_\beta = \frac{(1 + \beta^2)pr}{\beta p + r}. \quad (16)$$

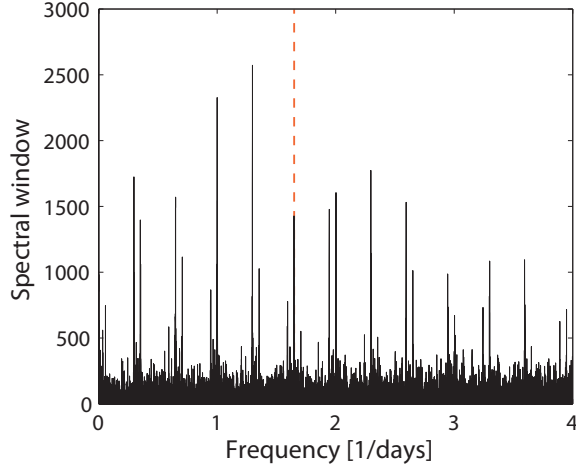


FIG. 9.— Spectral window of the tenth band from lightcurve lm0090m4818. The red dotted line shows the location of the underlying period ($1/P = 0.6485$). The underlying period is associated to the eighth highest local maximum of the spectrum.

The denominator of r in Eq. (15) corresponds to the number of periodic lightcurves in the dataset. Recall, is the ratio of recovered periodic lightcurves over the total number of periodic lightcurves in the dataset. The denominator of p in Eq. (15) corresponds to the number of lightcurves that are classified as periodic. Precision or completeness, is the ratio of recovered periodic lightcurves over the total amount of lightcurves that are classified as periodic. The F-score (Eq. 16) is a weighted average of recall and precision. The parameter β controls the importance of recall over precision on the weighted average. In what follows we use the F_1 score ($\beta = 1$).

We also define hit rate as:

$$HR = \frac{TP^*}{TP^* + FN}, \quad (17)$$

where TP^* are the periodic lightcurves classified as periodic and at the same time the true period is recovered⁹.

4. SYNTHETIC LIGHTCURVES

In order to evaluate the actual efficiency of the system and determine the true number of periodics in our dataset, we build a synthetic set containing both non-periodic and periodic lightcurves.

Periodic set: The periodic synthetic lightcurves are generated using a multivariate Gaussian generative model with a covariance matrix similar to the periodic kernel in eq. 8. To generate a periodic synthetic lightcurve, with period P , signal-to-noise ratio S , and smoothness σ we follow the procedure below.

1. Randomly select a lightcurve from the database and extract its time instants $\{t_i\}$ and error bars $\{e_i\}$. This defines the number of samples, N , of the generated lightcurve.
2. Use the time instants $\{t_i\}$, period P , smoothness

⁹ Note that a light curve can be classified as periodic even if the true period is not recovered, such as when a multiple of the true period is found.

σ and generate an $N \times N$ covariance matrix as,

$$\Sigma_1(i, j) = \frac{1}{\sqrt{2\pi}\sigma} \exp\left(-\frac{2\sin^2(\pi(t_i - t_j)/P)}{\sigma^2}\right).$$

3. Generate a random periodic vector, Y_s , of length N using a multivariate normal random generator with $N \times 1$ zero mean vector and Σ_1 covariance matrix.
4. Use the error bars to generate a $N \times N$ diagonal covariance matrix with diagonal elements,

$$\Sigma_2(i, i) = e_i^2$$

5. Generate a random noise vector Y_n of length N using a multivariate normal random generator with a $N \times 1$ zero mean vector and Σ_2 covariance matrix.
6. The synthetic lightcurve Y is obtained by summing the noise vector and the signal vector as follows

$$Y = S \frac{\text{med}(e_i)}{0.7413 \text{ iqr}(Y_s)} Y_s + Y_n, \quad (18)$$

where S is the desired signal-to-noise ratio, med is the median function and iqr is the interquartile range. Note that the resulting lightcurve has signal-to-noise ratio S by construction.

For our purpose we generated a set of 10,000 synthetic periodic lightcurves, using the following parameter ranges,

- Ten linearly spaced values for σ in the range $[0.1, 0.6]$.
- Twenty logarithmically spaced values for P in the range $[0.4, 1000]$ days.
- Ten values for S extracted from the distribution of the signal-to-noise ratio of EROS-2 lightcurves.

Five synthetic lightcurves are generated for each combination of S , P and σ .

We present examples of the synthetic lightcurves generated using this procedure in Fig 10. Fig 10a shows a synthetic lightcurve with a period of 2.432 days, a smoothness value of 0.2 and a SNR of 10. Using a low smoothness value yields a shape with many features. Due to the high SNR the periodicity is very clear. Fig 10b shows a synthetic lightcurve with a period of 10.42 days, smoothness of 0.5 and SNR of 4. In this case, a higher σ value yields a smoother shape as seen in the folded lightcurve. Fig 10c shows a synthetic lightcurve with a period of 154 days, smoothness of 0.4 and SNR of 2.

Non-periodic set: The non-periodic synthetic lightcurves are generated using block-bootstrap surrogates (Schmitz & Schreiber 1999; Schreiber & Schmitz 1999; Buhmann 1999). The procedure to generate a non-periodic synthetic lightcurve is as follows

1. Randomly select a lightcurve and extract its time instants $\{t_i\}$ and error bars $\{e_i\}$. This defines the number of samples N of the generated lightcurve.
2. Compute slotted autocorrelation function (ACF) (Edelson & Krolik 1988) of the lightcurve.

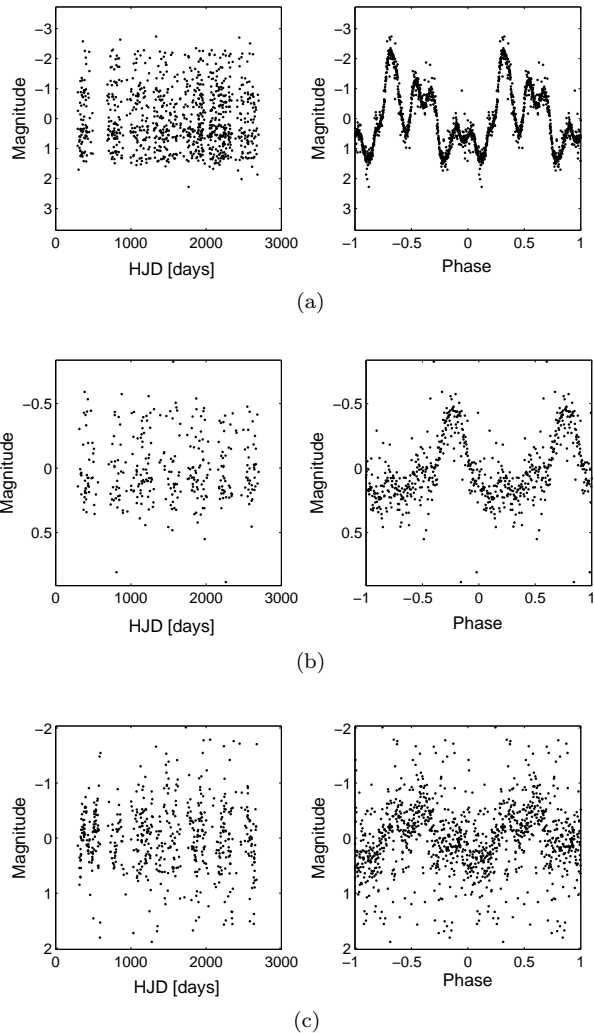


FIG. 10.— Example of a synthetic periodic lightcurves. (a) shows a lightcurve created using $P=2.432\text{d}$, $\sigma_t=0.2$, $\text{SNR}=10$ and $N=642$. (b) shows a lightcurve created using $P=10.24\text{d}$, $\sigma_t=0.5$, $\text{SNR}=4$ and $N=342$. (c) shows a lightcurve created using $P=154\text{d}$, $\sigma_t=0.4$, $\text{SNR}=2$ and $N=932$.

3. Find the time lag associated to the ACF value of $\exp(-1)$, this time lag is used as the block length (BL) for the block bootstrap method below.
4. Until at least N magnitude values have been created, do

- (a) Randomly select the block starting point i_s , such that $i_s \in [1, N - N']$. Find N' as the last lightcurve sample that complies with

$$t(N) - t(N') > BL$$

- (b) Find the end point of the block i_e as the first time instant that complies with

$$t(i_e + 1) - t(i_s) > BL$$

- (c) Grab the time instants, magnitudes, and error bars of the original lightcurve segment in $[i_s, i_e + 1]$.
- (d) Subtract the initial time t_{i_s} to the selected time instants. After this the block starts at zero days.

- (e) Add the time from the previous block t_{PB} to the selected time instants ($t_{PB} = 0$ for the first block). After this the block starts where the last block ended.
- (f) Update $t_{PB} = t(i_e + 1)$. Delete the time instant, magnitude and error bar of sample $i_e + 1$ from the block.
- (g) Add the newly constructed block to the surrogate.

For each EROS-2 lightcurve selected, ten surrogates were created. Ten thousand EROS-2 lightcurves were used to create a training set of 100,000 non-periodic synthetic lightcurves. To demonstrate that the resulting surrogates are not periodic and retain the same spectra characteristics as the originals lightcurves, we perform the procedure described above with a lightcurve of a periodic star. Fig 11a shows EROS-2 lightcurve lm0090127524 folded with a period of 0.337443 days. The associated CKP value is 2.7424. The block bootstrap method was used to create a non-periodic synthetic lightcurve. Fig. 11b shows the slotted ACF and the block length selected for this lightcurve is 3.67 days. Ten surrogates are generated using the procedure described above. Fig. 11c shows one of the surrogates. The surrogate is folded with its best period and clearly the periodicity of the original lightcurve is not retained by the surrogate.

4.1. Obtaining the periodicity discrimination thresholds

A lightcurve is labelled as periodic if the CKP value associated to its best trial period is above a given periodicity discrimination threshold. We determine the threshold by optimizing the F_1 score (Eq. 16) with a training set created as described above and following the guidelines in Section 3.2. The periodicity threshold is a function of the SNR and therefore we obtain a periodicity threshold per SNR. To do so, the SNR values are discretized in eight bins: $S = \{[0, 1.5], [1.5, 2], [2, 2.5], [2.5, 3.5], [3.5, 5], [5, 10], [10, 20], [20, \infty]\}$ and compute the periodicity threshold according to the following procedure:

- Evaluate the CKP values for each lightcurve in the training set whose SNR fall in bin S .
- Construct a threshold array of 5000 points in $[\min(\text{CKP}), \max(\text{CKP})]$.
- Compute the F_1 score (Eq. 16) at each threshold value.
- Select the threshold $th(S)$ as the CKP value that maximizes the F_1 score.

Once the thresholds have been computed, a lightcurve whose SNR falls in bin S is labelled as periodic if:

$$CKP(P_{best}) > th(S),$$

where P_{best} is the detected period that maximizes the CKP for the given lightcurve.

4.2. Estimating the true number of periodic lightcurves

In this section we elaborate on how to estimate the number of periodic lightcurves in a dataset. This is not to be confused with the number of lightcurves labeled as periodic by the proposed method. The true number of periodic lightcurves in a dataset, N_p , is the number of true positives plus the false negatives, which is equivalent to the denominator of r in Eq. (15). The number of

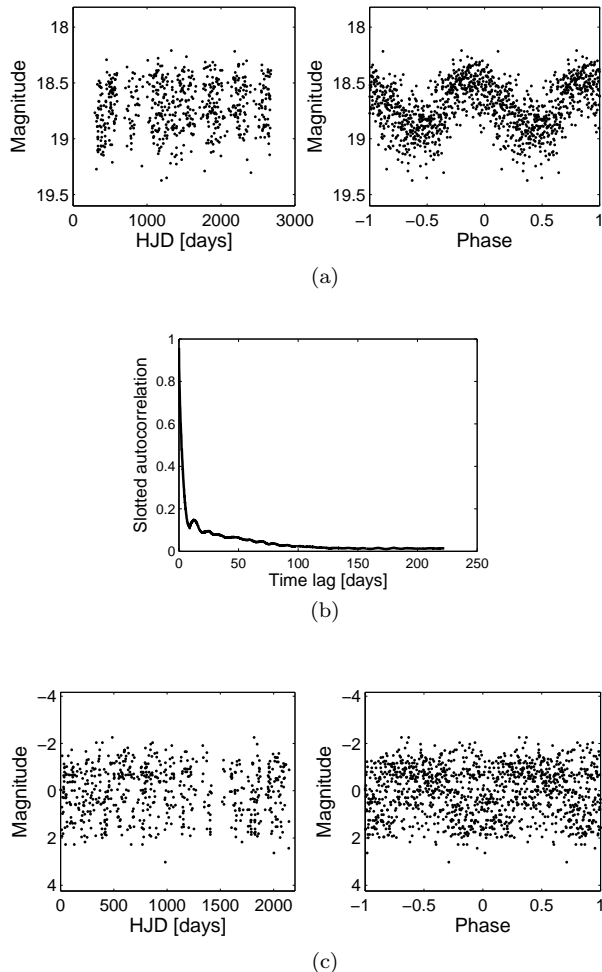


FIG. 11.— (a) Periodic lightcurve EROS-2 lm0090127524 folded with the period of 0.337443 days, this period has a CKP value of 2.7424. (b) Slotted autocorrelation function of lightcurve lm0090127524. Using the slotted ACF, a window length of 3.67 days is selected to create the surrogates. (c) A surrogate created from lm0090127524. The CKP value of the surrogate is 0.4532, which is below the corresponding periodicity threshold.

lightcurves classified as periodics, \tilde{N}_p , is the number of true positives plus false positives, which is equivalent to the denominator of p in Eq. (15).

Using Eq. (15) we can estimate the actual number of periodics in a given SNR bin S as

$$N_p(S) = \tilde{N}_p(S) \frac{p(S)}{r(S)}, \quad (19)$$

where $p(S)$ and $r(S)$ are the precision and recall values for bin S , respectively, which we assume we can determine from the training set. The precision and recall values are computed following the procedure given in Section 4.1. Given an \tilde{N}_p , we can estimate the true number of periodic lightcurves in a dataset as:

$$\tilde{N}_p = \sum_S \tilde{N}_p(S) \frac{p(S)}{r(S)}, \quad (20)$$

Table 1 shows the thresholds $th(S)$ and associated F-score, recall and precision values obtained for each SNR bin S . The overall precision and recall (across the SNR

TABLE 1
PERIODICITY THRESHOLDS AND ASSOCIATED PRECISION AND RECALL VALUES FOR EACH SNR BIN.

S	th(S)	max F-score	p(S) [%]	r(S) [%]
[0, 1.5]	0.4584	0.92	94.26	89.15
[1.5, 2]	0.4565	0.94	95.14	92.15
[2, 2.5]	0.4537	0.95	96.42	92.98
[2.5, 3.5]	0.4581	0.96	96.82	94.26
[3.5, 5]	0.5875	0.97	97.52	96.12
[5, 10]	1.1153	0.98	98.12	97.51
[10, 20]	1.6464	0.98	98.22	97.81
[20, ∞]	2.4112	0.97	98.54	96.15

bins) are 95.3% and 92.7%, respectively.

4.3. Efficiency as a function of parameters

In the following tests we assess the efficiency of the proposed method as a function of the parameters of the synthetic lightcurves. Hit rate (Eq. 17) is measured as a function of the total time span divided by the period, number of samples, smoothness, and SNR for the 10,000 synthetic periodic lightcurves. Hit rates are computed as a function of one of the parameters while summing for the other three. The CKP is compared with the LS periodogram on each test.

Fig. 12a shows a plot of the HR as a function of the ratio between the total time span of the lightcurve and its period (T/P). The total time span of the lightcurves in EROS-2 survey is approximately 2500 days, and the sampling rate is approximately 1.2 samples per day. The ratio T/P can be viewed as the number of times the underlying signal repeats itself. The period range in the training set goes from 0.4 days to 1000 days. HR is stable across the given range except for T/P below 10 and above 2300. Intuitively, the fewer times a signal is repeated across T the more difficult it is to assess its periodicity. This can be seen in the plot for periods above 280 days. There is also a limit in the resolution due by the sampling rate, which is reflected as a hit rate drop for periods below 0.5 days. The same hit rate drop can be observed for the LS periodogram.

Fig. 12b shows a plot of HR as a function of the number of samples of the synthetic lightcurve. HR increases with the number of samples. The hit rate rises by 5% when the number of samples increases from 300 to 600. In comparison with the LS periodogram, the CKP is less affected by N . Intuitively, the less information available on the process the harder it is to assess its periodicity.

Fig. 12c shows a plot of the hit rate as a function of the smoothness (σ) of the synthetic lightcurves. The hit rate is stable across the given range, decreasing slowly for the very large and very small values of σ . Overall, the smoothness does not have great influence on the CKP hit rate. The LS-periodogram hit rate increases with σ . This is expected, as smaller values of σ produce lightcurves with highly non-sinusoidal shapes, as shown in Fig. 10a10b, 10c.

Finally, Fig. 12d shows a plot of the hit rate as a function of the SNR (Eq. 22) of the synthetic lightcurves. HR is stable for the given SNR range, dropping abruptly for SNR below 1.8. For SNR of 1.2 hit rate has decreased by a almost 25%. A similar behaviour can be seen for the LS-periodogram.

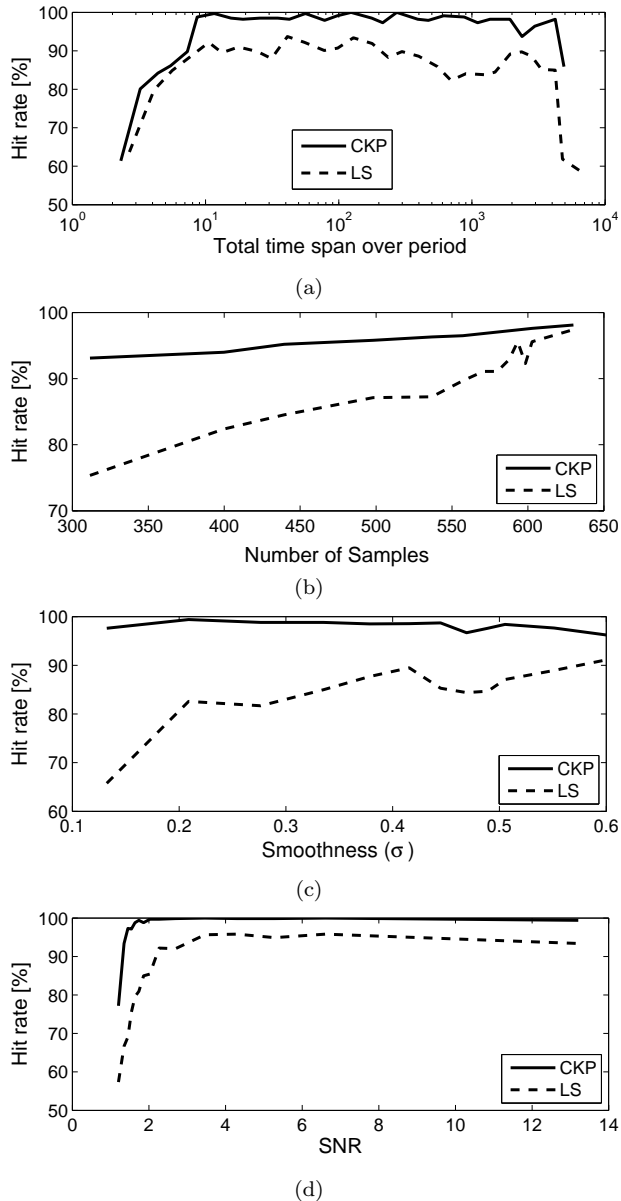


FIG. 12.— Hit rate in the synthetic periodic lightcurves as a function of the value of the parameters used to generate the set. The parameters are the number of samples (a), the smoothness (b), period over total time span (c), and SNR (d). The proposed method is compared with the LS periodogram.

5. DATA

5.1. Description of the data

The EROS-2 project (Tisserand et al. 2007; Rahal et al. 2009) was designed to search for gravitational microlensing events caused by massive compact halo objects (MACHOs) in the halo of the Milky Way. To do this, 32.8 million stars in the Magellanic clouds were surveyed over 6.7 years. The objective of the EROS-2 survey was to test the hypothesis that MACHOs were a major component of the dark matter present in the Halo of our galaxy.

The EROS-2 project surveyed 28.8 million stars in the Large Magellanic Cloud (LMC) and 4 million stars in the Small Magellanic Cloud (SMC), distributed in 88 and 10 observational fields, respectively. Each field is divided

in 32 chips (8 CCDs and 4 quadrants per CCD). Each lightcurve file has 5 columns: time instant, red channel magnitude, red channel error bars, blue channel magnitude and blue channel error bars. In what follows, only the blue channel is used. The average number of samples per lightcurve is 430 and 780 in the LMC and SMC, respectively.

5.2. Preprocessing and intricacies of the data

Fixing the error bars: As described above the kernel size was estimated using the errorbars of the magnitudes or the estimate of the observational errors. If these observational errors were underestimated or overestimated (as is often the case) the kernel size will be also wrongly-estimated. For example if the error bars are for some reason underestimated then the kernel bandwidth will be also underestimated and will not account of the true scatter of the lightcurve resulting into low CKP values.

For a lightcurve that is not variable the sample variance and the error bars should have very similar values. Another way of expressing this is that for a given non-variable lightcurve the median of the error bars should be equal to the inter-quartile range. Since we know most sources are not variable a plot of those two quantities should be distributed around the bisector¹⁰. Fig. 13a shows a plot of the median of the error bars as a function of the interquartile range of the magnitudes for a randomly selected chip, lm0090k. Each dot corresponds to a lightcurve. The locus of the points (lightcurves with magnitudes between 17 and 21) is over the bisector, *i.e.* the error bars are larger than the dispersion of the lightcurve. This is an example of a field with overestimated error bars.

For a given field with N_{lc} lightcurves, the error bar *correction factor* is defined as the constant that minimizes

$$\alpha_{cf} = \arg \min_{\alpha} \sum_{k=1}^{N_{lc}} (\text{iqr}(\{y\}_k) - \alpha \text{med}(\{e\}_k))^2, \quad (21)$$

where $\{y\}_k$ and $\{e\}_k$ are the magnitudes and error bars of lightcurve k , respectively, *iqr* is the interquartile range and *med* is the median.

For the field shown in Fig. 13a an error bar correction factor of 0.42 is obtained for this field. Fig. 13b shows the plot of the same field after correcting the error bars. Fig. 14 shows the same plot for chip lm0140k. This chip is on the periphery of the LMC. The error bar correction factor for this field is ~ 1 , *i.e.* there is no need for correction.

Using the error bar correction factor, we define the pseudo signal-to-noise-ratio (pSNR) of a given lightcurve as

$$pSNR = \frac{0.7413 \text{iqr}(\{y\})}{\alpha \text{med}(\{e\})}, \quad (22)$$

where y and e are the magnitudes and error bars, respectively, and α is computed per field using Eq. 21.

Removing outliers and bad points: The mean \bar{e} and the standard deviation σ_e of the error bars are computed per lightcurve and samples that do not comply with

$$e_i < \bar{e} + 3\sigma_e,$$

¹⁰ Line with slope of one.

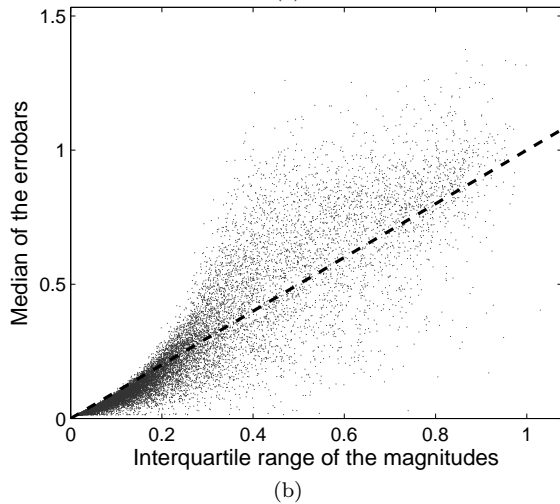
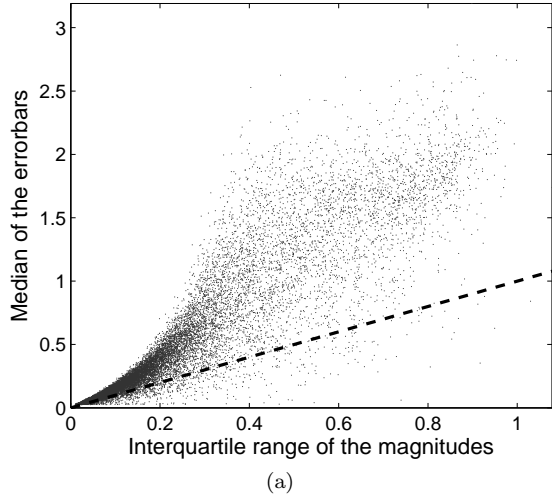


FIG. 13.— (a) Median of the magnitude’s error bars as a function of the interquartile range of the magnitudes for chip lm0090k. The dotted line has a slope of one. The error bar correction factor for lm0090k is 0.42. (b) The same plot after correcting the error bars.

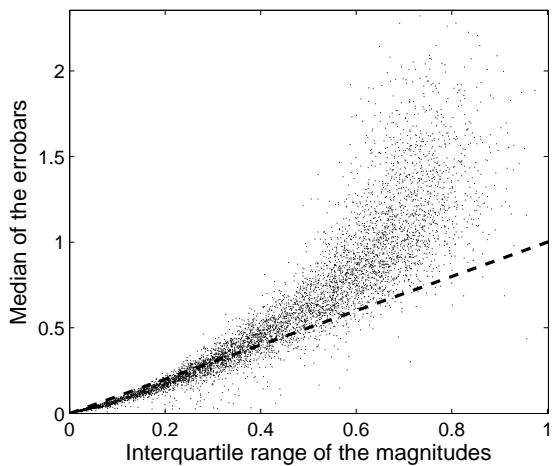


FIG. 14.— Median of the magnitude’s error bars as a function of the interquartile range of the magnitudes for chip lm0140k. The error bar correction factor for lm0140k is ~ 1 .

where e_i is the error bar of a sample i , are removed from the lightcurve. At this point, lightcurves with less than fifty samples are discarded from the analysis.

TABLE 2
DESCRIPTION OF THE SPURIOUS PERIODS

Period [days]	Description
1	Solar day (P_d)
29.5305	Moon phase or Synodic month (P_m)
365.24	Tropical year (P_y)
2,335	Average time span of EROS-2 lightcurves (T)
0.4917	$((P_d/2)^{-1} + P_m^{-1})^{-1}$
0.5086	$((P_d/2)^{-1} - P_m^{-1})^{-1}$
0.9672	$(P_d^{-1} + P_m^{-1})^{-1}$
1.0351	Lunar day, $(P_d^{-1} - P_m^{-1})^{-1}$
0.9973	Sidereal day, $(P_d^{-1} + P_y^{-1})^{-1}$
1.0027	$(P_d^{-1} - P_y^{-1})^{-1}$
27.31	Sidereal month, $(P_m^{-1} + P_y^{-1})^{-1}$
32.13	$(P_m^{-1} - P_y^{-1})^{-1}$
315.65	$(P_y^{-1} + T^{-1})^{-1}$
432.63	$(P_y^{-1} - T^{-1})^{-1}$

Simple detrending: After that, the coefficients of a least square linear χ^2 regression on the magnitudes are computed

$$\chi^2 = \sum_{i=1}^N \frac{(a_0 + a_1 t_i - x_i)^2}{e_i^2}, \quad (23)$$

where a_0 is the intercept and a_1 is the slope. The coefficients of the linear fit are obtained by differentiating Eq. (23) wrt a_1 and a_0 . The linear χ^2 fit is subtracted from the lightcurve only if the correlation coefficient between the lightcurve and its linear fit is above 0.5 (goodness of fit). Fig. 15a shows EROS-2 lightcurve lm0324k13673. The signal is mounted on a monotonically increasing linear trend. The dotted line in Fig. 15a shows the χ^2 linear fit. Fig. 15b shows the lightcurve after the linear fit subtraction, further evaluation shows that the lightcurves is periodic with a period of 120.38 days.

6. RESULTS

6.1. Filtering of spurious periods

The trial periods extracted with the bands method are evaluated using the CKP (Eq. 13) contain spurious periods related to the solar day, the moon phase, the year, and their multiples are filtered. Additional spurious periods were found by analyzing the histogram of the periodic lightcurves detected by the proposed method (Fig. 16a). These additional spurious periods, which are given in Table 2, correspond to aliases of the known spurious periods.

A Gaussian mask centered around the spurious period is created for each of the spurious periods. Periods whose CKP fall inside the masks are filtered as spurious periods. The standard deviation and the amplitude of the masks are set so that the associated spurious peak in the period histogram is flattened¹¹. The trial period that maximizes the CKP and does not fall in any of the spurious period masks is selected as the best trial period for the lightcurve.

6.2. Results for selected fields

¹¹ The parameters of the filters can be found alongside the catalogs at <http://timemachine.iic.harvard.edu>

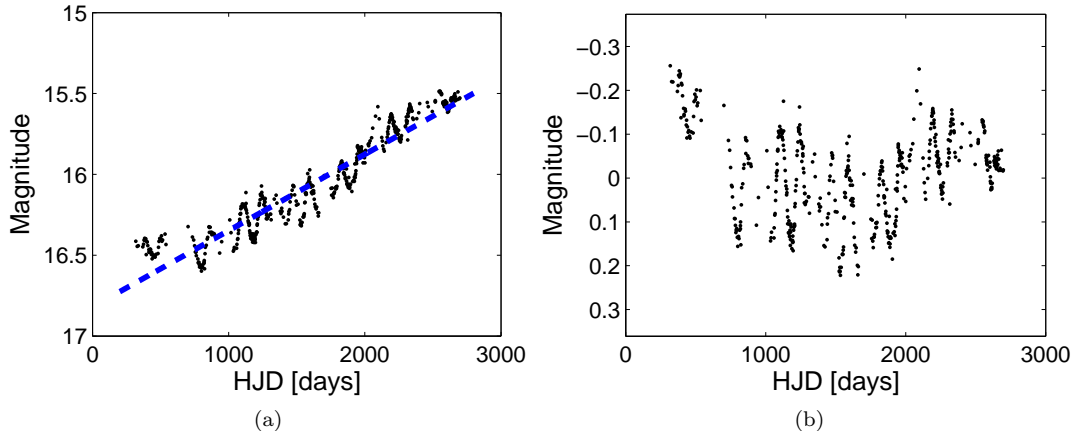


FIG. 15.— (a) Lightcurve lm0324k13673 from the EROS-2 survey. A linear χ^2 fit is computed for this lightcurve (blue dotted line). The correlation coefficient for the linear fit is 0.9493. (b) lightcurve lm0324k13673 after the linear trend subtraction.

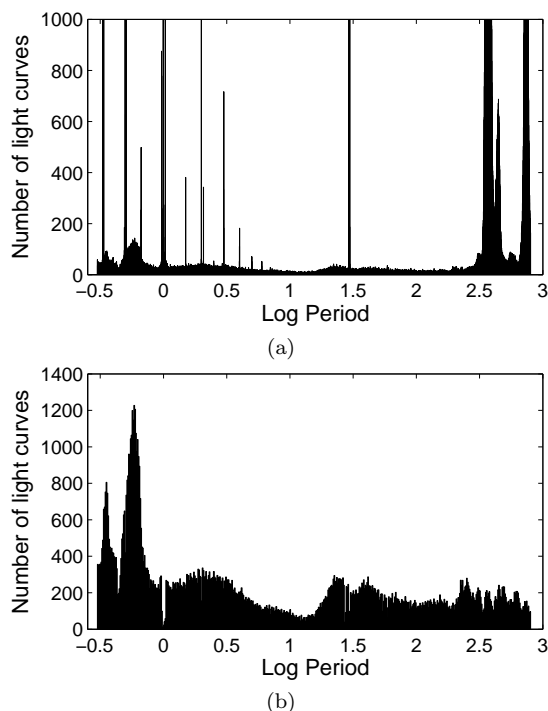


FIG. 16.— (a) Histogram of the periodic lightcurves detected with the proposed method on the LMC. The spurious periods have not been filtered in these results. The vertical columns corresponds to the spurious periods, their multiples and aliases. (b) Histogram of the periodic lightcurves detected in the LMC after carrying out the spurious period removal scheme.

In this experiment the proposed method is evaluated on three fields from the EROS-2 survey. The objectives are to measure the accuracy of the method and to compare the number of periodic lightcurves in the fields with the expected number of periodic lightcurves computed from the synthetic results by performing visual inspection to a large but manageable number of lightcurves. The first six chips from fields lm009, lm012 and sm001 are used in this experiment. Table 3 shows the number of lightcurves, the average number of samples and the average SNR from the selected fields.

Table 4 shows the results obtained for the selected fields. Column two (\tilde{N}_p) corresponds to the number of lightcurves labelled as periodic by our method. These

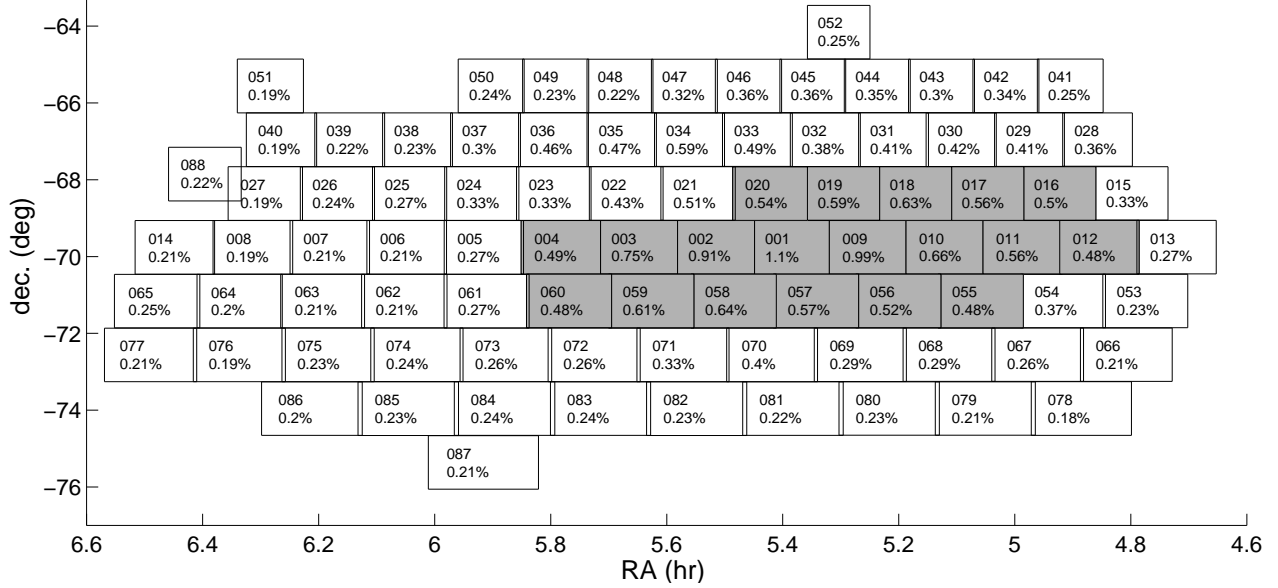
lightcurves are folded with the detected period and visually checked in order to find the number of false positives (column three). Column four is the precision in the detected periodic lightcurves set. Column five gives an estimate of the false negatives (FN) in the field. The FNs are estimated by visually inspecting the folded lightcurves of the objects that are below the periodicity thresholds. Because it is impracticable to check all the non-periodic objects, the search for FNs is stopped if 50 consecutive non-periodic lightcurves are found for each SNR bin. Column six is the recall calculated using the observed number of true positives ($\tilde{N}_p - \text{FP}$) and the FN. Column seven corresponds to the observed number of periodic lightcurves ($\tilde{N}_p - \text{FP} + \text{FN}$). Column eight shows an estimation of the true number of periodic variables (N_p) using the synthetic precision and recall values given in Section 4.2. Column seven is also an estimation of N_p because the true amount of FNs is not known.

A grand total of 1160 periodic lightcurves is recovered from field lm009, which corresponds to a 1.06% of the field. The percentage of periodic lightcurves in lm012 and sm001 is 0.75% and 1.69%, respectively¹². The overall precision and recall in all the fields is within 2% of the overall precision and recall found in the synthetic dataset. For comparison we ran the Lomb-Scargle periodogram¹³ on the lm009 field. The spurious periods are filtered as described in previous Sections. The filtered periods found with the LS periodogram are sorted according to their normalized LS statistic. By imposing a threshold on this statistic the periodic light curves obtained the CKP plus 298 false positives and 14 additional true positives are obtained. This corresponds to a drop of 16.5% in precision and a negligible increase in recall (1%) with respect to the CKP.

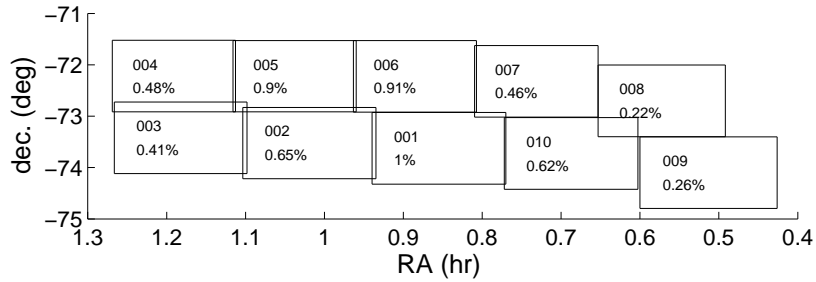
It is important to note that there are periodic behaviors that are not captured in the proposed synthetic lightcurve set. Examples of these are periodicities mounted on polynomial trends, objects with more than one oscillation period, objects that are not periodic in the whole time span and objects whose oscillations

¹² These chips have a higher number of periodics than the average found in the LMC and SMC as it can be seen in Fig. 17a. This issue is discussed in the next section.

¹³ The vartools software with the -LS option is used.



(a)



(b)

FIG. 17.— Maps of the EROS-2 LMC (a) and SMC (b) fields, respectively. The percentage of periodic lightcurves is shown below the name of the field.

amplitude change irregularly or following a modulation pattern, such as semi-regular and irregular LPVs. These cases are considered as non-periodic during the inspection. Examples of these cases are shown in Figures 18a, 18b and 18c, which correspond to false positives found in field lm009. Currently the proposed method is not able to discriminate quasi-periodicities and other irregular periodics.

TABLE 3
CHARACTERISTICS OF SELECTED FIELDS.

Field	Number of lightcurves	Average \bar{N}	Average SNR
lm009	109,802	548	1.628
lm012	95,010	447	0.959
sm001	92,666	830	1.505

6.3. Results on EROS-2 LMC and SMC fields

A total of 32.8 million lightcurves from the EROS-2 survey were processed with the proposed periodicity discrimination pipeline, 28.8 million from the LMC and 4 million from the SMC. Table 5 shows the summary of the results for the LMC and SMC. \tilde{N}_p corresponds to the number of lightcurves labeled as periodic by our method.

The *Discarded* column corresponds to the number of periodic lightcurves that appear twice in the list, due to field overlapping and blending. Column N_p corresponds to an estimation of the true number of periodic variables using the synthetic precision and recall values given in Section 4.2.

To select the ‘duplicate’ lightcurves, the nearest neighbor for each object in terms of angular distances is firstly identified. If the distance to the nearest neighbor is less than $10''$ and both objects have the same period, then the lightcurve with the lowest magnitude is added to the discarded set. Using this criterion 2663 pairs of lightcurves are selected from the LMC. From this set 336 correspond to lightcurves that reside in different chips. The average delta magnitude in this set is 0.281 and the average delta CKP is 0.744. Each pair of lightcurves correspond to the same star which appears twice in the survey due to the overlapping in the observational fields. The other 2327 cases correspond to lightcurves that are neighbours in the same chip. The average delta magnitude in this set is 2.15 and the average delta CKP is 3.02, much higher than the previous set. In this set the more luminous star of the pair injects its periodicity in the lightcurve of the less luminous star (blending). Fig. 19 shows an example of an overlapped pair and blended pair. It is interesting to note that a 72% of the blended lightcurves are

TABLE 4
RESULTS IN THE SELECTED EROS-2 SURVEY FIELDS.

Field	N_p	FP	Prec. [%]	FN	Recall [%]	Observed N_p	Synthetic N_p
lm009	1160	41	96.47	66	94.43	1185	1189
lm012	718	30	95.82	51	93.10	739	743
sm001	1564	69	95.59	99	93.79	1594	1637

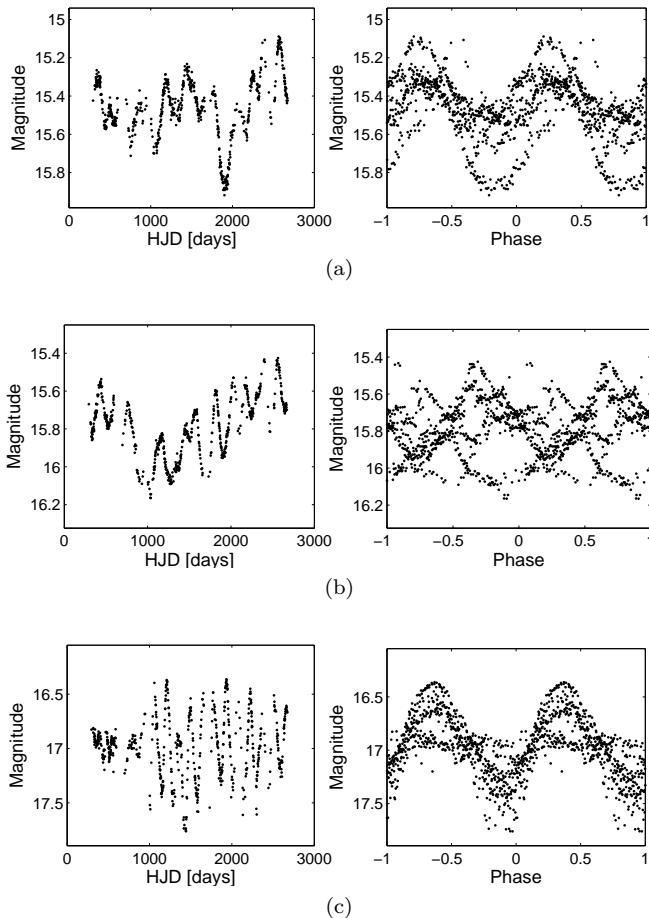


FIG. 18.— These lightcurves are examples of the false positives found in the catalogs. (a) lightcurve lm0090n29655, folded with the detected period of 278 days, is an example of quasi-periodic behaviour. (b) lightcurve lm0091119300, folded with the detected period of 264 days, is mounted on a polynomial trend in the mean. (c) lightcurve lm0090n6107, folded with the detected period of 144 days, varies in amplitude across the time span.

found in the fields within the LMC bar where the star density is the highest, while the overlapped lightcurves are equally distributed between bar and non bar fields. In the SMC 1817 pairs of lightcurves are selected to be discarded. In this case 386 are due to field overlapping and 1431 are due to blending. The average delta magnitude in the overlapped lightcurves is 0.21 and the average delta CKP is 0.78. The average delta magnitude in the blended lightcurves is 2.34 and the average delta CKP is 4.86. The percentage of discarded lightcurves in the SMC is 7.2% which is higher than the 2.3% found in the LMC. This again attributed to the fact that SMC seeing is worst than LMC resulting into overlapping PSF which in turn into correlated lightcurves.

Fig 17a shows a map of the 88 fields of the LMC. The shaded fields correspond to the LMC bar. The percent-

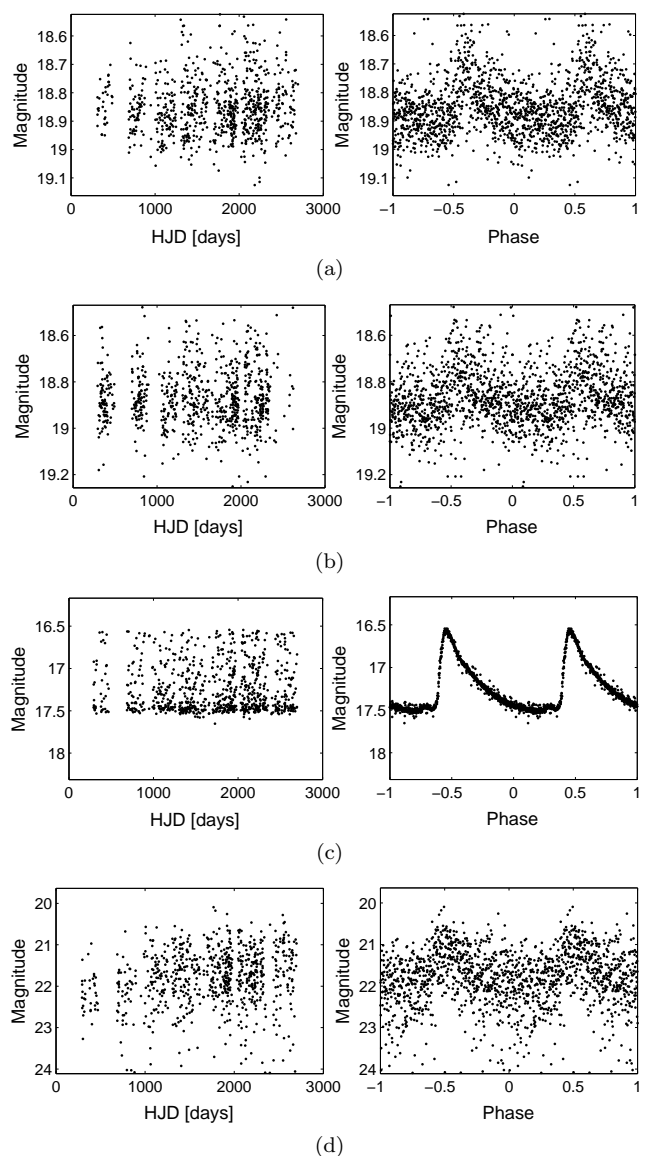


FIG. 19.— Examples of overlapping and blending. A period of 2.4796 days is detected for lightcurves sm0077n17908 (a) and sm0010k3199 (b). The angular distance between these lightcurves is $0.5''$. Their difference in magnitude and CKP value is 0.03 and 0.23, respectively. These lightcurves are associated to a star that is in an overlapped region between fields sm001 and sm007. Lightcurves sm0023n10183 (c) and sm0023n10325 (d) are also found to have the same period (1.2535 days), but they reside in the same field. Their angular distance, δ -magnitude and δ -CKP is $4.9''$, 4.5 and 4.1, respectively. In this case the light from sm0023n10183 (c) introduces a periodicity in its neighbour (d).

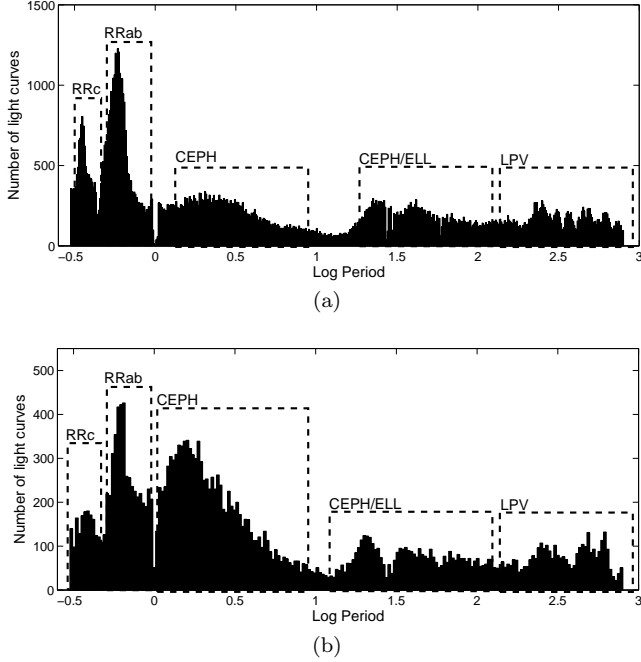


FIG. 20.— Histogram of the periods found in the LMC (a) and SMC (b) blue channel data. The regions marked with dotted boxes are associated to clusters of a given type periodic variable star.

age of periodic lightcurves is shown for each field below its name. The fields corresponding to the LMC bar have a higher percentage of periodics. The percentage of periodics tends to drop the further the field is from the LMC bar. Fig 17b shows a map of the 10 fields of the SMC where the same pattern is apparent. Because the cores of the LMCs have older population of stars it is known that one would expect more periodic stars in those regions.

A grand total of 118,320 and 23,103 periodic lightcurves are found from the LMC and SMC blue channel data, respectively. Using the recall and precision from the training dataset we estimate that the true number of periodic lightcurves is 121,147 for LMC and 24,855 for the SMC. A 0.42% of the lightcurves of the LMC are periodic and a 0.61% of the lightcurves in the SMC are periodic.

Fig. 20a shows the histogram of the periods found in the LMC blue channel data. Some of the known populations of periodic variables are identified in the histogram. The most notable populations correspond to c-type RR Lyrae (period centered in 0.3 days) and ab-type RR Lyrae (period centered in 0.6 days). These results are consistent with the RR Lyrae period histogram from the MACHO survey results on the LMC (Cook et al. 1995).

Fig. 21a shows a color magnitude diagram of the periodic lightcurves found in the LMC blue channel. The third axis corresponds to the detected period. The regions of interest are marked with black dotted squares. Examples of the periodic variable stars found in these regions are shown in Fig. 29 through 32. These results are consistent with the color magnitude diagram of the LMC periodic variables from the OGLE survey (Spano et al. 2009).

Fig. 20b and 21b show the histogram of periods and the color magnitude diagram of the periodic lightcurves found in the SMC blue channel, respectively. By comparing the histogram and color magnitude diagram with

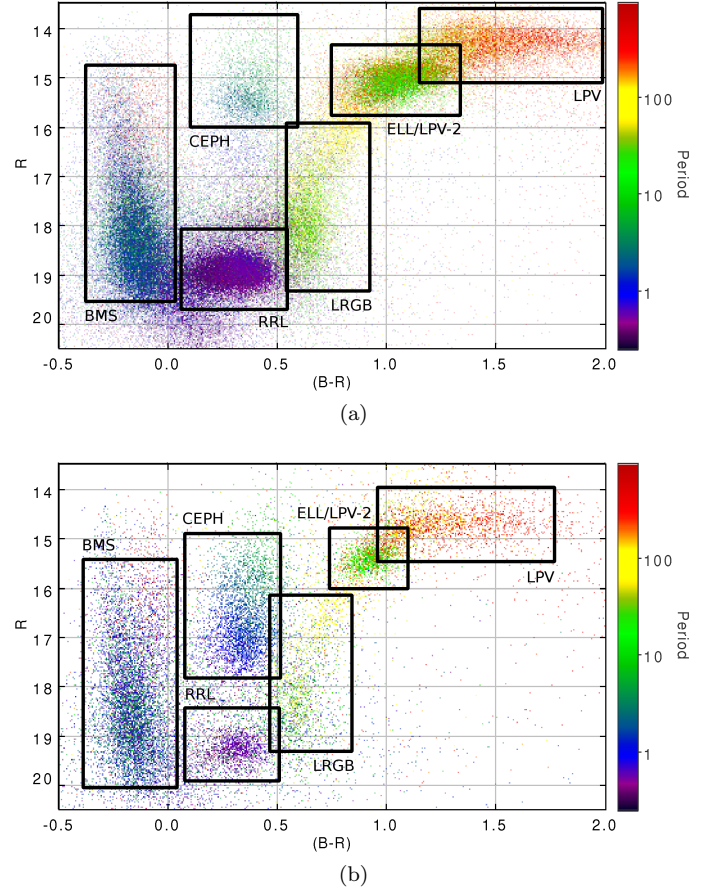


FIG. 21.— Color magnitude diagram showing the periodic lightcurves found in the LMC (a) and SMC (b). BMS corresponds to blue main sequence. LRGB corresponds to lower red giant branch. Black boxes mark the location of Cepheid, RR Lyrae, LPV and ellipsoidal variable populations.

those of the LMC, the following differences arise: the relative size of the Cepheid population is larger in the SMC, the relative size of the c-type RR Lyrae population is larger in the LMC.

The red channel lightcurves are also analyzed for comparison purposes. A grand total of 87,025 and 14,501 periodic lightcurves are collected from the LMC and SMC red channel data, respectively. This represents a decrease of 30% with respect to the amount of periodics collected from the blue channel. By cross-matching the lists obtained from the blue and red channels in the LMC we found that 68,179 objects appear in both lists, 50,141 objects are found only in the blue channel, and 18,846 objects are found only in the red channel. For the SMC, 12,536 objects appear in both lists, 1,965 appear exclusively in the red and 10,567 appear exclusively in the blue. For a given object the SNR may change between channels as shown in the examples of Fig. 22. By inspecting the histogram of the color $(B - R)_{eros}$ of the EROS-2 lightcurves, it is clear that it is skewed to the blue side. The average color value in the LMC and SMC is 0.46 and 0.31, respectively and therefore the SNR is higher in the blue channel and therefore this explains why more periodics are found in the blue channel data¹⁴.

¹⁴ Another reason could be related to the training scheme, in which only blue channel lightcurves were used to create the syn-

TABLE 5
PERIODIC LIGHTCURVE DISCRIMINATION RESULTS SUMMARY ON THE EROS-2 SURVEY.

	N_{LC}	N_p	Discarded	N_p	Periodics [%]
LMC	28,797,305	120,983	2,663	121,147	0.42
SMC	4,064,179	24,920	1,817	24,855	0.61

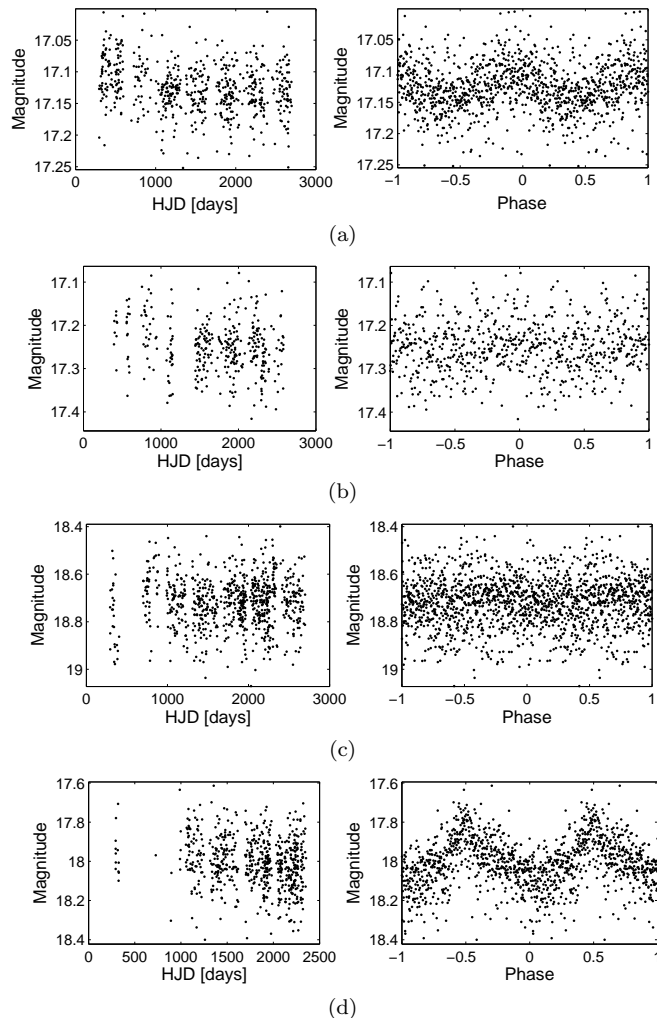


FIG. 22.— Examples of periodic lightcurves detected only in one of the EROS-2 channels. Fig (a) and (b) correspond to lightcurve lm0012k17912. Fig (a) shows the blue channel lightcurve folded with the detected period of 0.48004 days. Using the red channel data no strong periodicity is found. Fig (b) shows red channel lightcurve folded with the 0.48004 days periods. Fig. (c) and (d) correspond to lightcurve sm0010l10270. Fig. (d) shows the red channel data folded with the detected period of 10.4453 days. Using the blue channel data no strong periodicity is found. Fig. (c) shows the blue channel data folded with the period detected in the red channel.

The catalogs are compared with existing periodic variable star catalogs for the LMC and SMC. We first test against the published OGLE catalogs for Cepheids (Soszyński et al. 2008; Soszyński et al. 2010a), type II Cepheids (Soszyński et al. 2008; Soszyński et al. 2010c), RR Lyrae (Soszyński et al. 2009; Soszyński et al. 2010b) and LPV (Soszyński et al. 2009; Soszyński et al. 2011) in the LMC and SMC. The OGLE team performed an extent period search using Fourier based methods, analytic database.

ysis of variance and visual inspection. In this test the objective is to reveal how many of the periodic variables reported by the OGLE team can be found in our catalogs and to analyze the discrepancies between the detected periods. Table 6 summarizes the results of the crossmatching. First, for each OGLE object, a nearest neighbor in the EROS catalog is found. Neighbors with a separation larger than 1.5 arcsec are not considered. Column N_{inEROS} corresponds to the number of OGLE objects that were found in the EROS set within the search distance. The OGLE objects that did not have an EROS neighbor were either out of EROS bounds, located on inter-chip EROS zones or located on corrupted EROS chips. Column N_{match} correspond to the number of crossmatched OGLE-EROS objects that appear in our periodic variable catalog. The differences between N_{inEROS} and N_{match} are due to OGLE objects whose CKP is below the periodicity threshold (low SNR light curves). There are cases in which the true period is within the spurious filters areas and was missed in our search. Finally the periods reported by OGLE are compared to the periods found with the our method. The agreement column corresponds to the percentage of lightcurves in which the OGLE period is equal to the period found in our catalog (a 1% relative error is considered). The multiple column corresponds to the cases in which the reported period is either a multiple, sub-multiple or alias of the OGLE period. The disagreement column corresponds to the cases in which the reported period is not related to the OGLE period.

There is a high level of agreement between the reported and OGLE periods for Cepheids, type II Cepheids and RR Lyrae classes, in both the LMC and SMC. The periods labeled as multiples were visually inspected. In these cases the OGLE period is the correct period, but it was not found by the proposed method because it was either below 0.3 days or filtered in the spurious period rejection stage. Examples of the lightcurves in which the reported period is in disagreement with the OGLE period are shown in Fig. 23.

For the LPV class the difference between N_{inEROS} and N_{match} is larger than in other classes (i.e. more objects with CKP below periodicity threshold). This is expected as the LPVs are known to suffer from irregularities that affect their period. Additionally, the level of agreement between periods is lower than the other classes. Fig. 24 shows examples of disagreeing periods in the LPV class.

There are 80,304 objects in our periodic catalog that do not have a neighbor from the OGLE periodic variable catalogs (within 2.5 arcsec). Some of these objects may have not been surveyed by the OGLE project, or they could belong to classes with currently not available catalogs such as eclipsing binaries. A 60% of these light curves have a low CKP value which translates roughly to low SNR. This could indicate that the proposed method is more sensitive than the method used by the OGLE team. Fig. 25 shows examples of periodic light curves

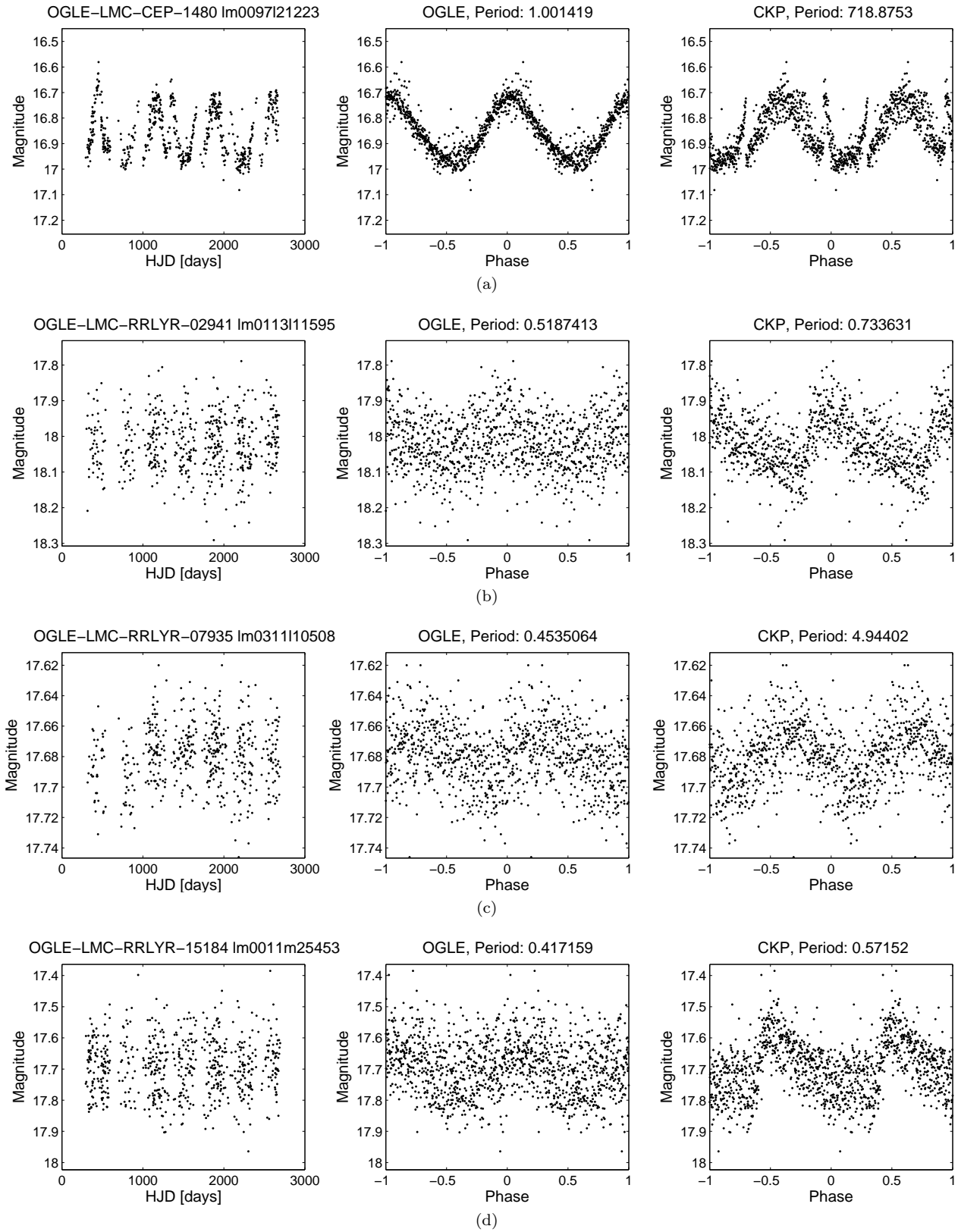


FIG. 23.— Light curves in which the reported period is in disagreement with the OGLE period. The EROS and OGLE labels, along the periods are shown in the title of each light curve.

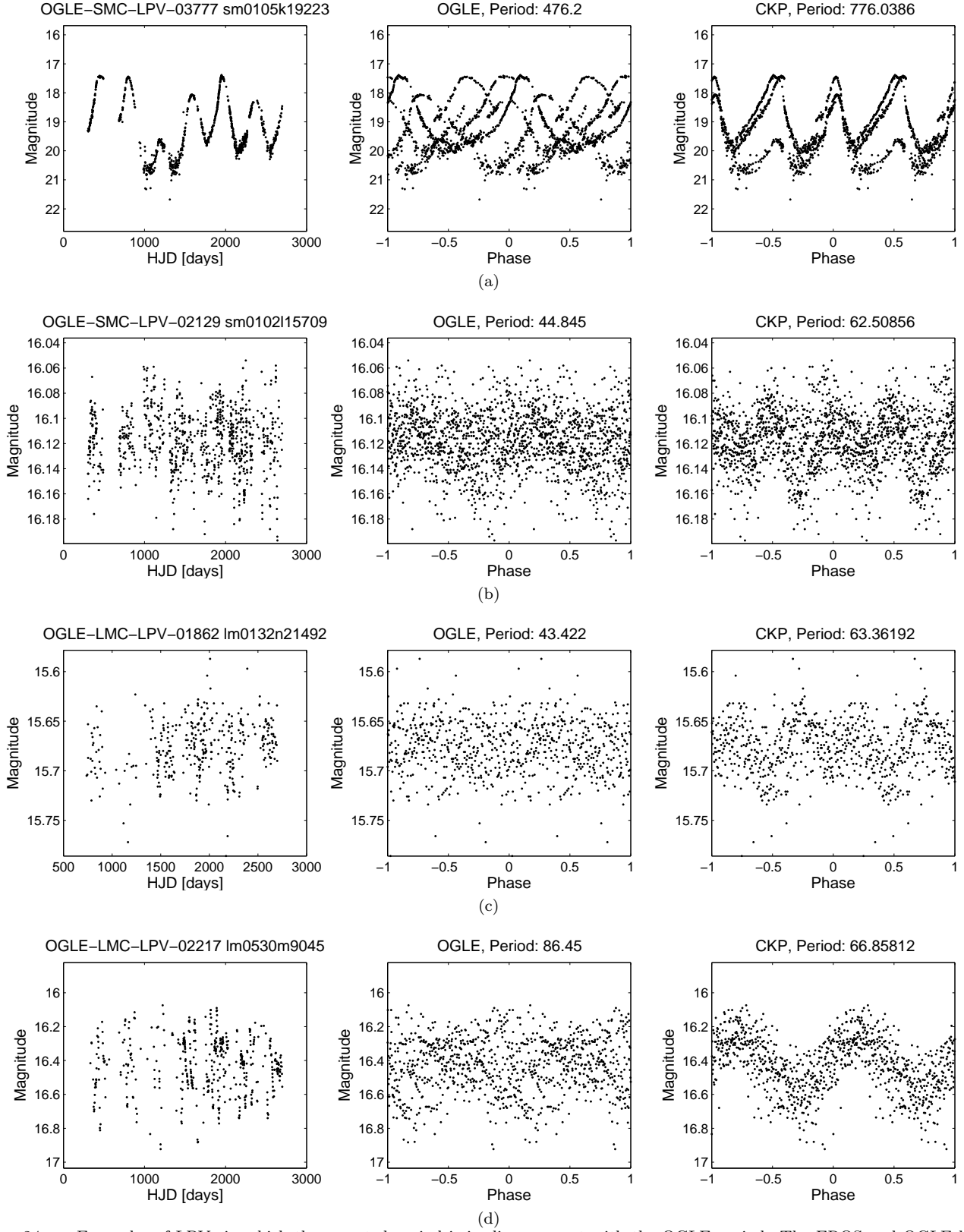


FIG. 24.— Examples of LPVs in which the reported period is in disagreement with the OGLE period. The EROS and OGLE labels, along the periods are shown in the title of each light curve.

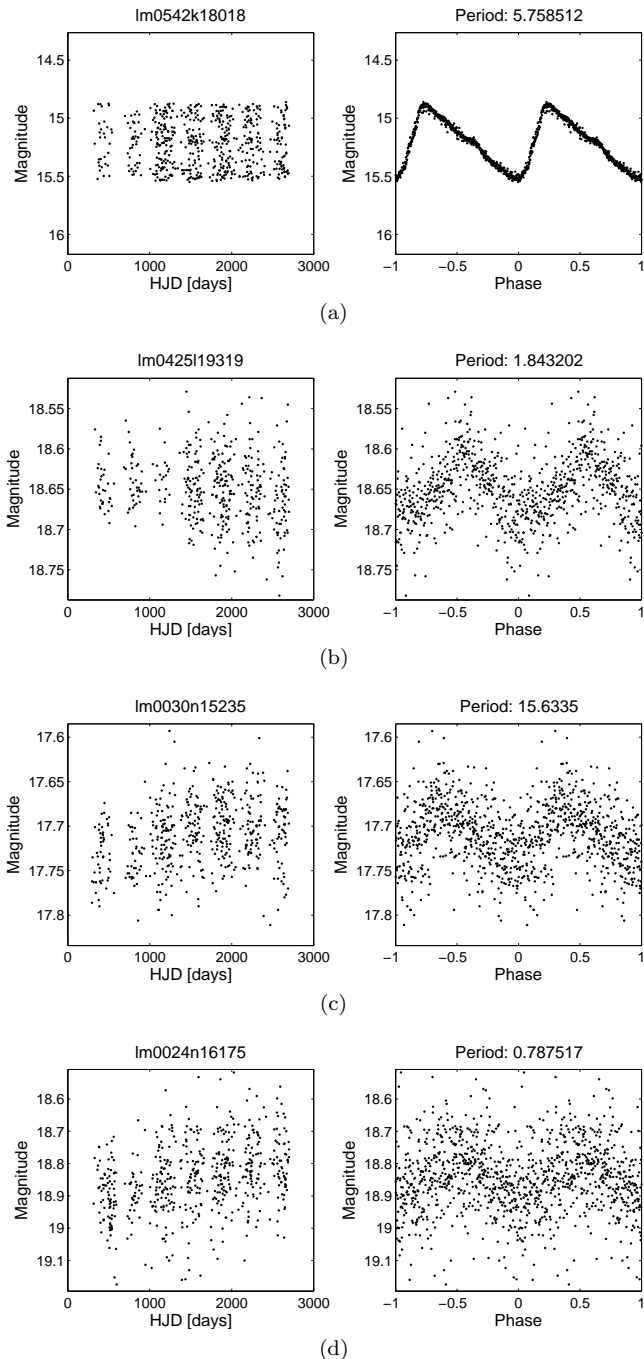


FIG. 25.— Examples of periodic light curves not found by OGLE. Fig (a) corresponds to a Cepheid variable with high SNR not found by OGLE. The majority of these light curves have a low CKP value which translates roughly to low SNR. Figures (b), (c) and (d) are low SNR examples.

found in the EROS catalog that do not appear in the OGLE catalogs.

The periodic variable catalogs are also compared to the lists of beat Cepheids found in the EROS-2 data by Marquette et al. (2009). The catalog contain Cepheids pulsating on their fundamental and first overtone (F/FO) and first and second overtone (FO/SO), respectively. The periods were obtained using a combination of Fourier decomposition, Analysis of Variance and visual inspection. The results are summarized in Table 7. There are eight cases that do not appear in our catalog due to their

CKP value being below the threshold. In the remaining 409 cases, only three cases show disagreement with the reported period. The one case in which the period is not a multiple of the EROS-2 period was shown in Fig. 23a.

7. BEYOND CKP

7.1. Multimodes

It is known that periodic stars exhibit multimode oscillations which is manifested in the morphology of the lightcurves. Despite the fact that the methodology presented in this paper was not designed to find multimodes, we have explored the multimodes in a two level search approach. For each periodic lightcurve the prime lightcurve P_0 is used to ‘remove’ the periodic signal. This procedure is known as whitening and is performed as follows:

1. Fold the light curve with P_0 .
2. Obtain a template of the periodicity by smoothing the folded light curve using a moving average of 30 samples.
3. Subtract the template from the folded light curve.
4. Rearrange the light curve samples to their original time order.

If the whitened lightcurve is found to be periodic with period P_1 , that is not multiple/sub-multiple or alias of P_0 , then the light curve is selected as a dual mode candidate. Subsequent oscillation modes can be found by repeating the procedure above.

This procedure is applied on 34,000 periodic light curves from the LMC with CKP values above 2.0¹⁵. From this set 1165 light curves are selected as dual mode candidates. After evaluating the double mode candidates, 116 are found to have a third oscillation mode. Examples of dual mode and triple mode candidates are shown in Figures 26 and 27, respectively. The lists of double and triple mode candidates can be found at <http://timemachine.iic.harvard.edu>.

Fig. 28 shows a Petersen diagram of the 1165 light curves selected as dual modes candidates. The triangles in the plot mark the 116 light curves in which a third mode was found. The periods are sorted so that $P_0 > P_1$ in all cases. The triple mode candidates occupy two horizontal lines at period ratios of 0.72 and 0.8. These values are close to the known ratios associated to the first and second overtones (Moskalik 2013). A prominent horizontal line appears at $P_1/P_0 \sim 2/3$ for fundamental periods above 10 days. According to Smolec et al. (2012) this ratio is associated to the period doubling phenomenon. Another interesting feature, shown in the lower left part of the diagram, are two curves that follow an inversely proportional relationship between the period ratio and fundamental period.

7.2. Odd periodic stars

The method presented here is a not a classification method and therefore the method does not distinguish between types of periodic variables. Most of the periodic objects found in this work can be classified to known

¹⁵ We only selected the most prominent periodic lightcurves

TABLE 6
CROSSMATCHING WITH OGLE PERIODIC VARIABLE CATALOGS IN THE LMC AND SMC.

OGLE catalog	$N_{catalog}$	N_{inEROS}	N_{match}	Agree [%]	Multiple [%]	Disagree [%]
OGLE-LMC-CEPH	3,375	2,727	2,711	98.8	1.0	0.2
OGLE-LMC-t2CEPH	203	161	148	94.6	4.1	1.3
OGLE-LMC-RRLyrr	24,906	18,092	17,272	92.0	6.8	1.2
OGLE-LMC-LPV	91,995	74,960	20,430	77.2	2.0	20.8
OGLE-SMC-CEPH	4,630	3,413	3,395	99.3	0.6	0.1
OGLE-SMC-t2CEPH	43	30	30	93.4	3.3	3.3
OGLE-SMC-RRLyrr	2,475	1,392	1,360	97.7	1.7	0.6
OGLE-SMC-LPV	19,384	14,103	4,413	70.3	2.6	27.1

TABLE 7
CROSSMATCHING WITH EROS-2 BEAT CEPHEID CATALOGS FOR THE LMC AND SMC.

Beat Cepheids catalog	$N_{catalog}$	N_{match}	Agree [%]	Multiple [%]	Disagree [%]
F/FO pulsation	115	109	100.0	0.0	0.0
FO/SO pulsation	302	300	99.0	0.66	0.33

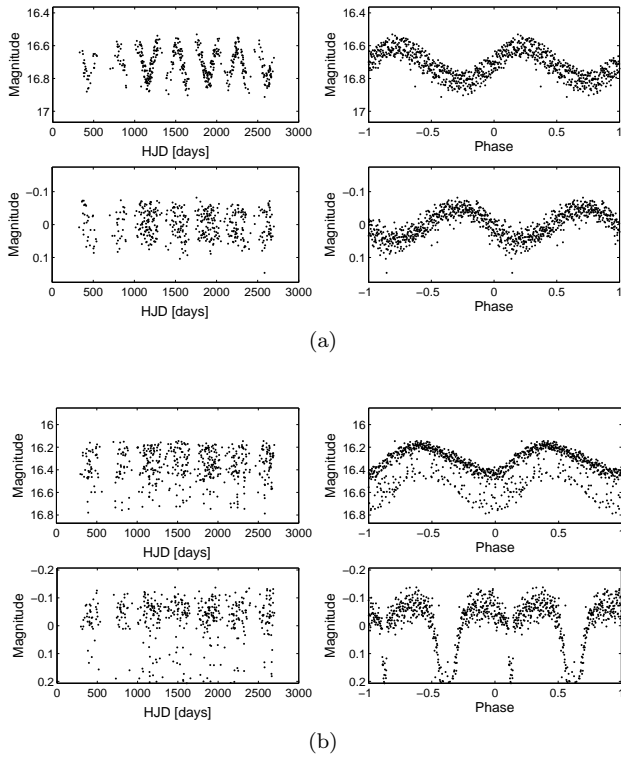


FIG. 26.— Light curves lm0356k24082 (a) and lm0100m7313 (b) are selected as dual mode candidates. On each plot, the first and second rows correspond to the original and whitened light curve, respectively. In (a) the original light curve is folded with $P_0 = 244.06$ days. The whitened light curve is folded with $P_1 = 3.6399$ days. In (b) the original light curve is folded with $P_0 = 6.3419$ days. The whitened light curve is folded with $P_1 = 84.19$ days.

classes as it is clearly shown in Figures 29, 30, 31 and 32. It is also expected that there should or could be stars with periodic behavior that does not fall in one of the known categories. It is the scope of a different paper to identify those rare or novel phenomena. Right here we only present a number of objects that we could not obviously attribute to any known classes or combination of classes. Figure 33 shows two such cases.

8. COMPUTATIONAL ISSUES

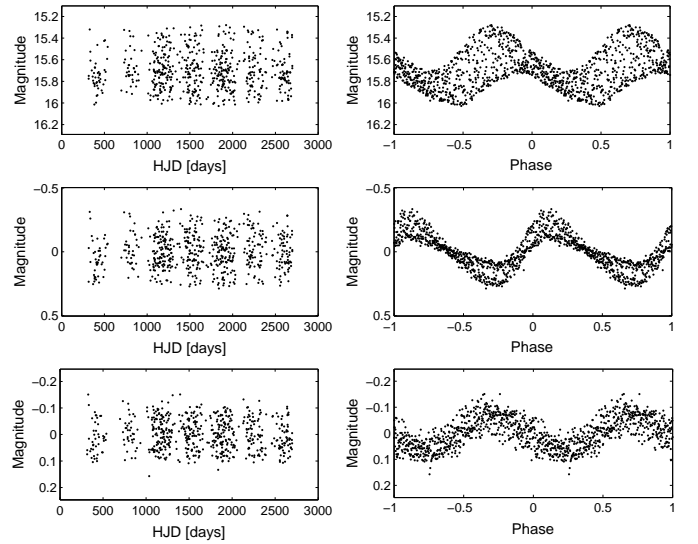


FIG. 27.— Light curve lm056518888 is selected as a triple mode candidate. In the plot the first, second and third rows correspond to the original, first whitened and second whitened light curves, respectively. The original light curve is folded with the detected period $P_0 = 2.4725$ days. The first whitened light curve is folded with $P_1 = 3.4455$ days. The second whitened light curve is folded with $P_2 = 1.4395$ days.

The proposed periodicity discrimination pipeline has been programmed for computational architectures based on graphical processing units (GPUs). The implementation is programmed in CUDA NVIDIA (2012), which is a variation of C developed by GPU manufacturer NVIDIA.

To evaluate the CKP metric (Eq. 10), one requires the $N(N-1)/2$ interactions between the N samples of the time series¹⁶. The CKP can be computed efficiently by mapping each of these interactions to a single GPU thread. The final value of the CKP is obtained through a $\log(N)$ -step sum reduction performed on the GPU. The

¹⁶ The kernel matrices given by Eq. (4) and Eq. (8) are symmetric, thus only the upper triangular part needs to be computed. The diagonal of the kernel matrices is constant and is omitted from the computations.

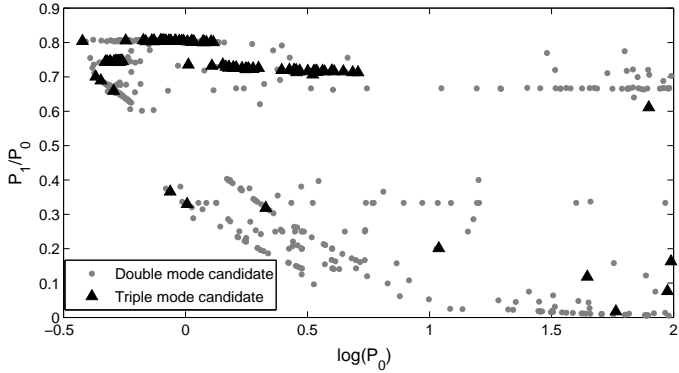


FIG. 28.— Petersen diagram of the 1165 dual mode candidates found in the LMC. The triangles mark the location of 116 triple mode candidates. Clear structures arise in the diagram.

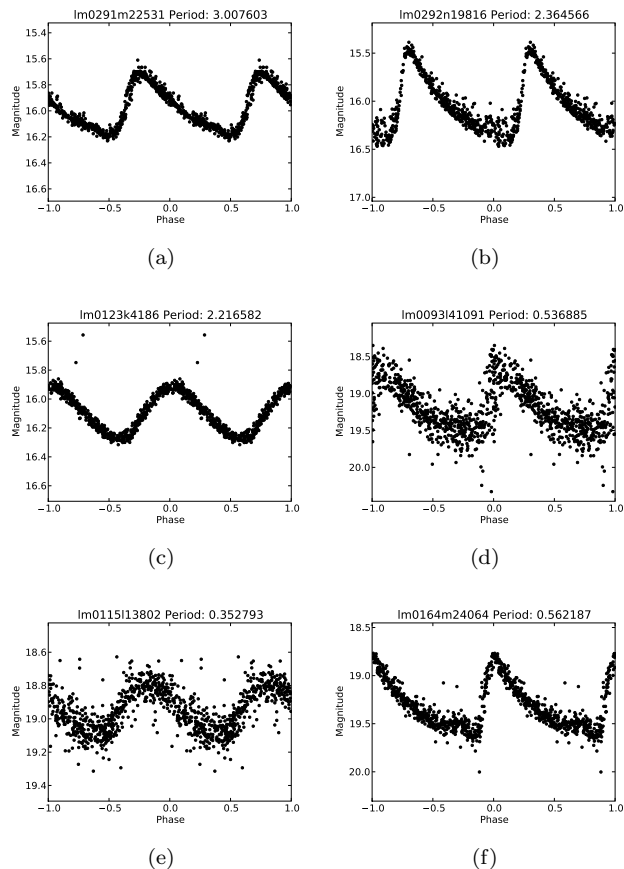


FIG. 29.— Examples of EROS-2 periodic lightcurves folded with their estimated period. (a), (b) and (c) are Cepheids taken from the CEPH cluster (see Fig. 21a). (d), (e) and (f) are RR Lyrae taken from the RRL cluster. (d) and (f) are examples of RRab class stars. (e) is an example of an RRc class star.

computational time required to analyze one lightcurve using our periodic discrimination pipeline is shown in Fig. 34. These times include the importation and transferring of the lightcurves to the GPU device. Times were measured on a NVIDIA Tesla C2070 GPU.

The 32.8 million lightcurves from the EROS-2 survey are processed on the NSCA Dell/NVIDIA cluster Forge. Forge is part of the Extreme Science and Engineering Discovery Environment (XSEDE). Forge has a total of

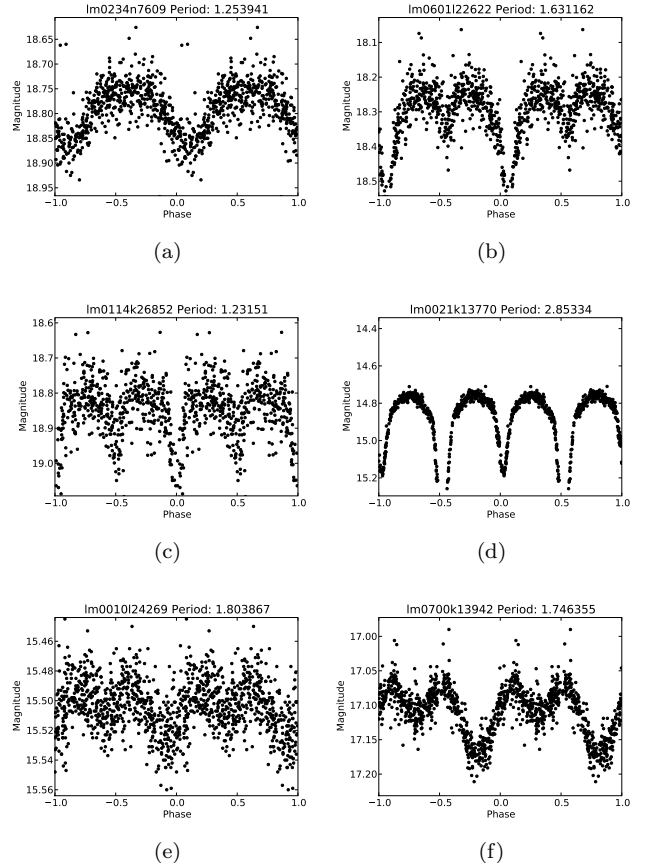


FIG. 30.— Examples of EROS-2 periodic lightcurves folded with their estimated period. These lightcurves corresponds to eclipsing binary stars found in the blue main sequence (see Fig. 21a).

TABLE 8

TOTAL COMPUTATIONAL TIME REQUIRED TO PROCESS THE 32.8 MILLION EROS-2 LIGHTCURVES (LMC PLUS SMC) ON XSEDE FORGE CLUSTER. GPUS IN ALL NODES ARE NVIDIA TESLA C2070.

Hardware	Computational time
Using 1 GPU	52.2 days
Using 6 GPUs (1 node)	8.71 days
Using 12 nodes (6 GPUs/node)	17.41 hours
Using all available nodes	7.28 hours

288 NVIDIA Tesla C2070 accelerators distributed on 44 nodes, however the maximum number of nodes that can be used at a time is 26. Each GPU process one chip from EROS-2. Table 8 shows the total computational time required to process the 32.8 million lightcurves from the LMC and SMC. These times does not include the time required to transfer the dataset to the cluster nor the time a job is waiting on the queue.

9. CONCLUSION

We presented and described a fully automated pipeline for periodic light curve discrimination. The method is based on the CKP, a robust information theoretic metric that discriminates periodic behavior by analyzing the similarities between lightcurve samples. The method is computational efficient; the pipeline takes 0.16 seconds to discriminate if a light curve is periodic or not. The

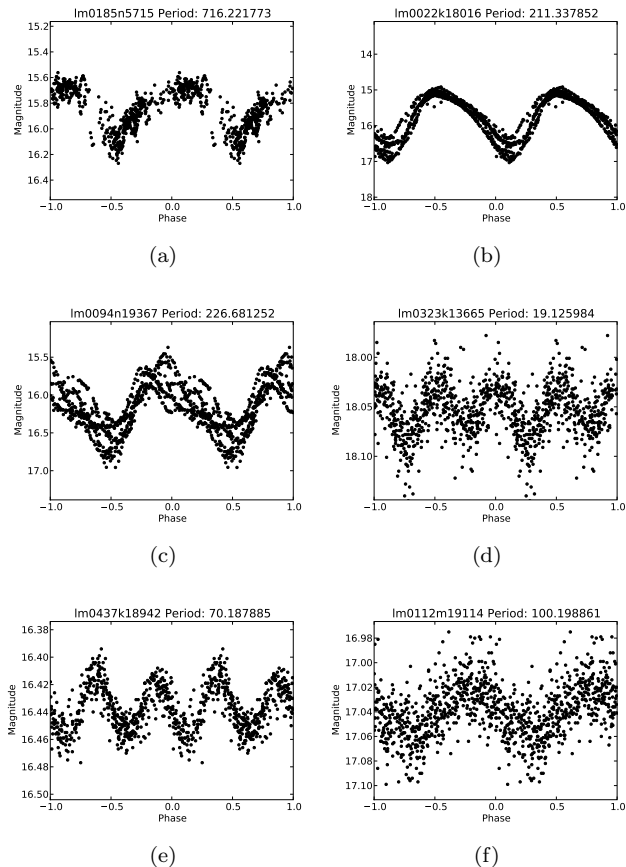


FIG. 31.— Examples of EROS-2 periodic lightcurves folded with their estimated period. (a), (b) and (c) correspond to long period variables found in the LPV cluster (see Fig. 21a). (d), (e) and (f) correspond to periodic variable stars found in the lower red giant branch.

32.8 million light curves were processed using a GPU cluster in less than 24 hours. This suggests that with few additional optimizations and up-to-date hardware the methods may scale well for modern and larger light curve databases.

The periodicity discrimination pipeline was tested on light curves from the EROS-2 survey. The methods were calibrated using synthetic time series that preserve the characteristics of EROS-2 light curves. The calibration procedure is general and it could be applied to other astronomical time series databases easily. In total 32.8 million light curves from the LMC and SMC were processed finding a grand total of 121,147 and 24,855 periodic variables in the LMC and SMC, respectively. The results obtained are consistent in terms of period distribution and localization of the periodic variables in the color-magnitude diagram. The observed results suggest that the periodic variable catalogues generated by our method could be used to find multimode variables and periodic variables that do not fall in any known category. It is also hinted that higher order analysis, such as stellar classification and clustering may be carried out straight-forwardly using the provided periods.

Using the synthetic dataset and visually inspecting a small subset of the dataset, we were able to characterize

the completeness and efficiency of the pipeline. We infer that 0.5% of the lightcurves with $\text{SNR} > 0.5$ are periodic.

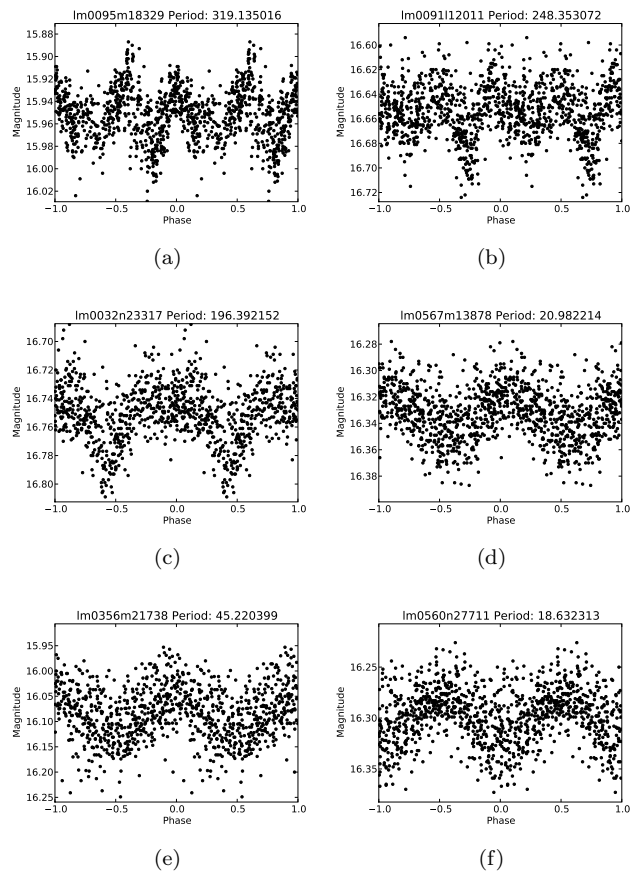


FIG. 32.— Examples of EROS-2 periodic lightcurves folded with their estimated period. (a), (b) and (c) correspond to long period variables found in the LPV-2 cluster (see Fig. 21a). (d), (e) and (f) correspond to ellipsoidal variables found in the ELL cluster.

Future work involves quasi-periodic and semi-regular behavior discrimination, more in-depth analysis of non-stationarities (trends) and developing more general kernel size selection schemes.

10. ACKNOWLEDGEMENT

This work was funded by CONICYT-CHILE under grant FONDECYT 1110701 and 1140816, and its Doctorate Scholarship program. Pablo Estévez acknowledges support from the Ministry of Economy, Development, and Tourism’s Millennium Science Initiative through grant IC12009, awarded to The Millennium Institute of Astrophysics, MAS.

The authors would like to thank the Harvard Institute for Applied Computational Science for providing research space and computing facilities.

The help received from the SEAS academic computing support staff and the time on the Harvard SEAS “Resonance” GPU cluster are greatly acknowledged.

This work used the Extreme Science and Engineering Discovery Environment (XSEDE), which is supported by National Science Foundation grant number OCI-1053575.

The EROS-2 project was funded by the CEA and the CNRS through the IN2P3 and INSU institutes. JBM acknowledges financial support from “Programme National de Physique Stellaire” (PNPS) of CNRS/INSU, France.

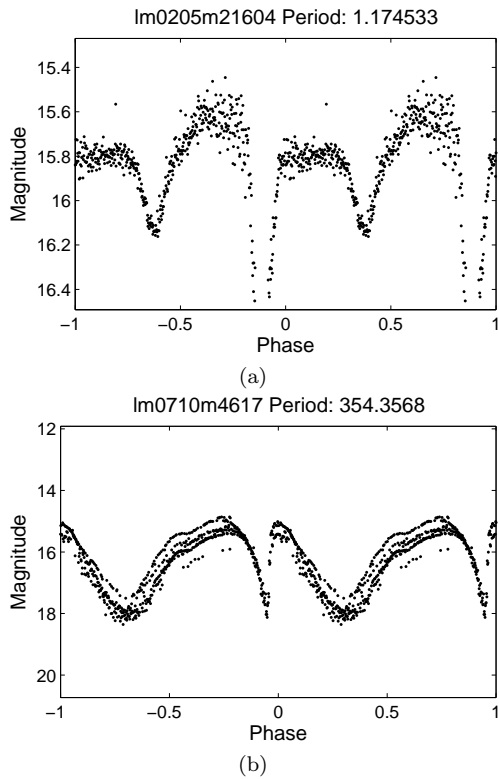


FIG. 33.— Examples of EROS-2 periodic lightcurves folded with their estimated period. A priori these objects cannot be attributed to any known class.

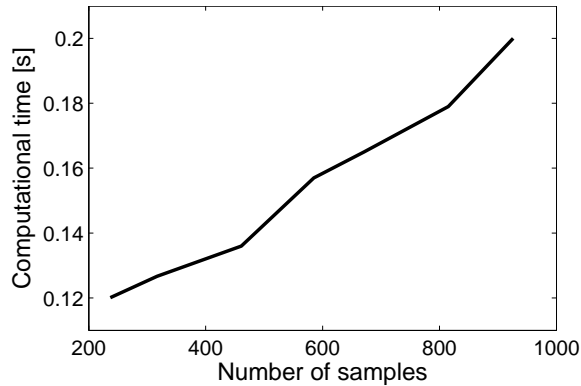


FIG. 34.— Computational time per lightcurve as a function of the number of samples

REFERENCES

- Alcock, C., Allsman, R. A., Alves, D. R., Axelrod, T. S., Becker, A. C., Bennett, D. P., Cook, K. H., Dalal, N., Drake, A. J., Freeman, K. C., Geha, M., Griest, K., Lehner, M. J., Marshall, S. L., Minniti, D., Nelson, C. A., Peterson, B. A., Popowski, P., Pratt, M. R., Quinn, P. J., Stubbs, C. W., Sutherland, W., Tomaney, A. B., Vandehei, T., & Welch, D. 2000, *The Astrophysical Journal*, 542, 281
- Buhlmann, P. 1999, *Statistical Science*, 17, 52
- Cook, K. H., Alcock, C., Allsman, H. A., Axelrod, T. S., Freeman, K. C., Peterson, B. A., Quinn, P. J., Rodgers, A. W., Bennett, D. P., Reimann, J., Griest, K., Marshall, S. L., Pratt, M. R., Stubbs, C. W., Sutherland, W., & Welch, D. L. 1995, in *Astronomical Society of the Pacific Conference Series*, Vol. 83, IAU Colloq. 155: *Astrophysical Applications of Stellar Pulsation*, ed. R. S. Stobie & P. A. Whitelock, 221
- Edelson, R. A., & Krolik, J. 1988, *The Astrophysical Journal*, 333, 646
- Eyer, L. 1999, *Baltic Astronomy*, 8, 321
- Hodapp, K. W., Kaiser, N., Aussel, H., Burgett, W., Chambers, K. C., Chun, M., Dombeck, T., Douglas, A., Hafner, D., Heasley, J., Hoblitt, J., Hude, C., Isani, S., Jedicke, R., Jewitt, D., Laux, U., Luppino, G. A., Lupton, R., Maberry, M., Magnier, E., Mannery, E., Monet, D., Morgan, J., Onaka, P., Price, P., Ryan, A., Siegmund, W., Szapudi, I., Tonry, J., Wainscoat, R., & Waterson, M. 2004, *Astronomische Nachrichten*, 325, 636
- Huijse, P., Estevez, P. A., Protopapas, P., Zegers, P., & Principe, J. C. 2012, *IEEE Transactions on Signal Processing*, 60, 5135

- Ivezic, Z., Tyson, J. A., Acosta, E., Allsman, R., Anderson, S. F., Andrew, J., Angel, R., Axelrod, T., Barr, J. D., Becker, A. C., Becla, J., Beldica, C., Blandford, R. D., Bloom, J. S., Borner, K., Brandt, W. N., Brown, M. E., Bullock, J. S., Burke, D. L., Chandrasekharan, S., Chesley, S., Claver, C. F., Connolly, A., Cook, K. H., Cooray, A., Covey, K. R., Cribbs, C., Cutri, R., Daus, G., Delgado, F., Ferguson, H., Gawiser, E., Geary, J. C., Gee, P., Geha, M., Gibson, R. R., Gilmore, D. K., Gressler, W. J., Hogg, C., Huffer, M. E., Jacoby, S. H., Jain, B., Jernigan, J. G., Jones, R. L., Juric, M., Kahn, S. M., Kalirai, J. S., Kantor, J. P., Kessler, R., Kirkby, D., Knox, L., Krabbendam, V. L., Krughoff, S., Kulkarni, S., Lambert, R., Levine, D., Liang, M., Lim, K., Lupton, R. H., Marshall, P., Marshall, S., May, M., Miller, M., Mills, D. J., Monet, D. G., Neill, D. R., Nordby, M., O'Connor, P., Oliver, J., Olivier, S. S., Olsen, K., Owen, R. E., Peterson, J. R., Petry, C. E., Pierfederici, F., Pietrowicz, S., Pike, R., Pinto, P. A., Plante, R., Radeka, V., Rasmussen, A., Ridgway, S. T., Rosing, W., Saha, A., Schalk, T. L., Schindler, R. H., Schneider, D. P., Schumacher, G., Sebag, J., Seppala, L. G., Shipsey, I., Silvestri, N., Smith, J. A., Smith, R. C., Strauss, M. A., Stubbs, C. W., Sweeney, D., Szalay, A., Thaler, J. J., Vanden Berk, D., Walkowicz, L., Warner, M., Willman, B., Wittman, D., Wolff, S. C., Wood-Vasey, W. M., Yoachim, P., Zhan, H., & for the LSST Collaboration. 2011, ArXiv e-prints, living document found at: <http://www.lsst.org/lsst/overview/>
- Jenkins, G. M., & Watts, D. G. 1968, Spectral analysis and its applications (Holden-day)
- Larson, S., Beshore, E., Hill, R., Christensen, E., McLean, D., Kolar, S., McNaught, R., & Garradd, G. 2003, in Bulletin of the American Astronomical Society, Vol. 35, AAS/Division for Planetary Sciences Meeting Abstracts #35, 982
- Law, N. M., Kulkarni, S. R., Dekany, R. G., Ofek, E. O., Quimby, R. M., Nugent, P. E., Surace, J., Grillmair, C. C., Bloom, J. S., Kasliwal, M. M., Bildsten, L., Brown, T., Cenko, S. B., Ciardi, D., Croner, E., Djorgovski, S. G., van Eyken, J., Filippenko, A. V., Fox, D. B., Gal-Yam, A., Hale, D., Hamam, N., Helou, G., Henning, J., Howell, D. A., Jacobsen, J., Laher, R., Mattingly, S., McKenna, D., Pickles, A., Poznanski, D., Rahmer, G., Rau, A., Rosing, W., Shara, M., Smith, R., Starr, D., Sullivan, M., Velur, V., Walters, R., & Zolkower, J. 2009, PASP, 121, 1395
- Mackay, D. 1998, Introduction to Gaussian Processes, Vol. 168 (Springer, Berlin), 133–165
- Marquardt, D., & Acuff, S. 1984, Direct Quadratic Spectrum Estimation with Irregularly Spaced Data (Springer-Verlag), 211–223
- Marquette, J. B., Beaulieu, J. P., Buchler, J. R., Szabó, R., Tisserand, P., Belghith, S., Fouqué, P., Lesquoy, É., Milsztajn, A., Schwarzenberg-Czerny, A., Afonso, C., Albert, J. N., Andersen, J., Ansari, R., Aubourg, É., Bareyre, P., Charlot, X., Coutures, C., Ferlet, R., Glicenstein, J. F., Goldman, B., Gould, A., Graff, D., Gros, M., Haïssinski, J., Hamadache, C., de Kat, J., Le Guillou, L., Loup, C., Magneville, C., Maurice, É., Maury, A., Moniez, M., Palanque-Delabrouille, N., Perdereau, O., Rahal, Y. R., Rich, J., Spiro, M., & Vidal-Madjar, A. 2009, A&A, 495, 249
- Michalak, M. 2010, in Computer Recognition Systems 4 (Berlin: Springer Verlag), 136–146
- Moskalik, P. 2013, in Advances in Solid State Physics, Vol. 31, Advances in Solid State Physics, ed. J. C. Suárez, R. Garrido, L. A. Balona, & J. Christensen-Dalsgaard, 103
- NVIDIA. 2012, CUDA C Programming Guide version 4.2 (NVIDIA)
- Principe, J. 2010, Information Theoretic Learning: Renyi's Entropy and Kernel Perspectives (New York: Springer Verlag)
- Rahal, Y. R., Afonso, C., Albert, J.-N., Andersen, J., Ansari, R., Aubourg, É., Bareyre, P., Beaulieu, J.-P., Charlot, X., Couchot, F., Coutures, C., Derue, F., Ferlet, R., Fouqué, P., Glicenstein, J.-F., Goldman, B., Gould, A., Graff, D., Gros, M., Haïssinski, J., Hamadache, C., de Kat, J., Lesquoy, É., Loup, C., Le Guillou, L., Magneville, C., Mansoux, B., Marquette, J.-B., Maurice, É., Maury, A., Milsztajn, A., Moniez, M., Palanque-Delabrouille, N., Perdereau, O., Rahvar, S., Rich, J., Spiro, M., Tisserand, P., Vidal-Madjar, A., & EROS-2 Collaboration. 2009, Astronomy & Astrophysics, 500, 1027
- Rasmussen, C. E., & Williams, C. K. I. 2006, Gaussian processes for machine learning (MIT Press)
- Reimann, J. D. 1994, Frequency Estimation Using Unequally-Spaced Astronomical Data (University of California, Berkeley)
- Scargle, J. 1982, The Astrophysical Journal, 263, 835
- Schmitz, A., & Schreiber, T. 1999, Phys. Rev. E, 59, 4044
- Schreiber, T., & Schmitz, A. 1999, Physica D: Nonlinear Phenomena, 142, 346
- Schölkopf, B., & Smola, A. 2002, Learning with Kernels (Cambridge, MA: Cambridge, MA: MIT Press)
- Smolec, R., Soszyński, I., Moskalik, P., Udalski, A., Szymański, M. K., Kubiak, M., Pietrzyński, G., Wyrzykowski, L., Ulaczyk, K., Poleski, R., Kozłowski, S., & Pietrukowicz, P. 2012, MNRAS, 419, 2407
- Soszyński, I., Poleski, R., Udalski, A., Szymański, M. K., Kubiak, M., Pietrzyński, G., Wyrzykowski, L., Szewczyk, O., & Ulaczyk, K. 2010a, Acta Astron, 60, 17
- Soszyński, I., Udalski, A., Szymański, M. K., Kubiak, J., Pietrzyński, G., Wyrzykowski, L., Ulaczyk, K., & Poleski, R. 2010b, Acta Astron, 60, 165
- Soszyński, I., Udalski, A., Szymański, M. K., Kubiak, M., Pietrzyński, G., Wyrzykowski, L., Szewczyk, O., Ulaczyk, K., & Poleski, R. 2009, Acta Astron, 59, 239
- Soszyński, I., Udalski, A., Szymański, M. K., Kubiak, M., Pietrzyński, G., Wyrzykowski, L., Ulaczyk, K., & Poleski, R. 2010c, Acta Astron, 60, 91
- Soszyński, I., Poleski, R., Udalski, A., Szymanski, M. K., Kubiak, M., Pietrzyński, G., Wyrzykowski, L., Szewczyk, O., & Ulaczyk, K. 2008, Acta Astron, 58, 163
- Soszyński, I., Udalski, A., Szymański, M. K., Kubiak, M., Pietrzyński, G., Wyrzykowski, L., Szewczyk, O., Ulaczyk, K., & Poleski, R. 2008, Acta Astron, 58, 293
- 2009, Acta Astron, 59, 1
- Soszyński, I., Udalski, A., Szymański, M. K., Kubiak, M., Pietrzyński, G., Wyrzykowski, L., Ulaczyk, K., Poleski, R., Kozłowski, S., & Pietrukowicz, P. 2011, Acta Astron, 61, 217
- Spano, M., Mowlavi, N., Eyer, L., & Burki, G. 2009, in American Institute of Physics Conference Series, Vol. 1170, American Institute of Physics Conference Series, ed. J. A. Guzik & P. A. Bradley, 324–326
- Stellingwerf, R. 1978, The Astrophysical Journal, 224, 953
- Taylor, J. S., & Cristianini, N. 2004, Kernel Methods for Pattern Analysis (Cambridge University Press)
- Tisserand, P., Le Guillou, L., Afonso, C., Albert, J. N., Andersen, J., Ansari, R., Aubourg, É., Bareyre, P., Beaulieu, J. P., Charlot, X., Coutures, C., Ferlet, R., Fouqué, P., Glicenstein, J. F., Goldman, B., Gould, A., Graff, D., Gros, M., Haïssinski, J., Hamadache, C., de Kat, J., Lasserre, T., Lesquoy, É., Loup, C., Magneville, C., Marquette, J. B., Maurice, É., Maury, A., Milsztajn, A., Moniez, M., Palanque-Delabrouille, N., Perdereau, O., Rahal, Y. R., Rich, J., Spiro, M., Vidal-Madjar, A., Vigroux, L., Zylberajch, S., & EROS-2 Collaboration. 2007, Astronomy & Astrophysics, 496, 387
- Udalski, A., Kubiak, M., & Szymanski, M. 1997, Acta Astronomica, 47, 319
- Wang, Y., Khardon, R., & Protopapas, P. 2012, ApJ, 756, 67

York, D. G., Adelman, J., Anderson, Jr., J. E., Anderson, S. F., Annis, J., Bahcall, N. A., Bakken, J. A., Barkhouser, R., Bastian, S., Berman, E., Boroski, W. N., Bracker, S., Briegel, C., Briggs, J. W., Brinkmann, J., Brunner, R., Burles, S., Carey, L., Carr, M. A., Castander, F. J., Chen, B., Colestock, P. L., Connolly, A. J., Crocker, J. H., Csabai, I., Czarapata, P. C., Davis, J. E., Doi, M., Dombeck, T., Eisenstein, D., Ellman, N., Elms, B. R., Evans, M. L., Fan, X., Federwitz, G. R., Fiscelli, L., Friedman, S., Frieman, J. A., Fukugita, M., Gillespie, B., Gunn, J. E., Gurbani, V. K., de Haas, E., Haldeman, M., Harris, F. H., Hayes, J., Heckman, T. M., Hennessy, G. S., Hindsley, R. B., Holm, S., Holmgren, D. J., Huang, C.-h., Hull, C., Husby, D., Ichikawa, S.-I., Ichikawa, T., Ivezić, Z., Kent, S., Kim, R. S. J., Kinney, E., Klaene, M., Kleinman, A. N., Kleinman, S., Knapp, G. R., Korienek, J., Kron, R. G., Kunszt, P. Z., Lamb, D. Q., Lee, B., Leger, R. F., Limmongkol, S., Lindenmeyer, C., Long, D. C., Loomis, C., Loveday, J., Lucinio, R., Lupton, R. H., MacKinnon, B., Mannery, E. J., Mantsch, P. M., Margon, B., McGehee, P., McKay, T. A., Meiksin, A., Merelli, A., Monet, D. G., Munn, J. A., Narayanan, V. K., Nash, T., Neilsen, E., Neswold, R., Newberg, H. J., Nichol, R. C., Nicinski, T., Nonino, M., Okada, N., Okamura, S., Ostriker, J. P., Owen, R., Pauls, A. G., Peoples, J., Peterson, R. L., Petravick, D., Pier, J. R., Pope, A., Pordes, R., Prosapio, A., Rechenmacher, R., Quinn, T. R., Richards, G. T., Richmond, M. W., Rivetta, C. H., Rockosi, C. M., Ruthmansdorfer, K., Sandford, D., Schlegel, D. J., Schneider, D. P., Sekiguchi, M., Sergey, G., Shimasaku, K., Siegmund, W. A., Smee, S., Smith, J. A., Snedden, S., Stone, R., Stoughton, C., Strauss, M. A., Stubbs, C., SubbaRao, M., Szalay, A. S., Szapudi, I., Szokoly, G. P., Thakar, A. R., Tremonti, C., Tucker, D. L., Uomoto, A., Vanden Berk, D., Vogeley, M. S., Waddell, P., Wang, S.-i., Watanabe, M., Weinberg, D. H., Yanny, B., Yasuda, N., & SDSS Collaboration. 2000, *The Astronomical Journal*, 120, 1579